

Revisiting the Color-Color Selection: Submillimeter and AGN Properties of NUV-r-J Selected Quiescent Galaxies

YU-HSUAN HWANG,^{1,2} WEI-HAO WANG,² YU-YEN CHANG,^{2,3} CHEN-FATT LIM,^{2,1} CHIAN-CHOU CHEN,² ZHEN-KAI GAO,^{4,2}
JAMES S. DUNLOP,⁵ YU GAO,^{6,7} LUIS C. HO,^{8,9} HO SEONG HWANG,^{10,11} MACIEJ KOPROWSKI,¹²
MICHAŁ J. MICHAŁOWSKI,¹³ YING-JIE PENG,⁸ HYUNJIN SHIM,¹⁴ JAMES M. SIMPSON,^{15,2,16} AND YOSHIKI TOBA^{17,2,18}

¹*Physics Department, National Taiwan University, No. 1, Sec. 4, Roosevelt Rd., Taipei 10617, Taiwan*

²*Academia Sinica Institute of Astronomy and Astrophysics, No. 1, Sec. 4, Roosevelt Rd., Taipei 10617, Taiwan*

³*Department of Physics, National Chung Hsing University, 40227, Taichung, Taiwan*

⁴*Graduate Institute of Astronomy, National Central University, Taiwan*

⁵*Institute for Astronomy, University of Edinburgh, Royal Observatory, Edinburgh EH9 3HJ, UK*

⁶*Department of Astronomy, Xiamen University, 422 Siming South Road, Xiamen 361005, People's Republic of China*

⁷*Purple Mountain Observatory/Key Laboratory for Radio Astronomy, Chinese Academy of Sciences, 10 Yuanhua Road, Nanjing 210023, People's Republic of China*

⁸*Kavli Institute for Astronomy and Astrophysics, Peking University, Beijing 100871, Peoples Republic of China*

⁹*Department of Astronomy, School of Physics, Peking University, Beijing 100871, Peoples Republic of China*

¹⁰*Korea Astronomy and Space Science Institute, 776 Daedeokdae-ro, Yuseong-gu, Daejeon 34055, Republic of Korea*

¹¹*Astronomy Program, Department of Physics and Astronomy, Seoul National University, 1 Gwanak-ro, Gwanak-gu, Seoul 08826, Republic of Korea*

¹²*Institute of Astronomy, Faculty of Physics, Astronomy and Informatics, Nicolaus Copernicus University, Grudziadzka 5, 87-100 Torun, Poland*

¹³*Astronomical Observatory Institute, Faculty of Physics, Adam Mickiewicz University, 60-286 Poznań, Poland*

¹⁴*Department of Earth Science Education, Kyungpook National University, Deagu 702-701, Republic of Korea*

¹⁵*Centre for Extragalactic Astronomy, Department of Physics, Durham University, UK*

¹⁶*National Astronomical Observatory of Japan, Japan*

¹⁷*Department of Astronomy, Kyoto University, Kitashirakawa-Oiwake-cho, Sakyo-ku, Kyoto 606-8502, Japan*

¹⁸*Research Center for Space and Cosmic Evolution, Ehime University, 2-5 Bunkyo-cho, Matsuyama, Ehime 790-8577, Japan*

(Received XX YY, ZZZZ; Revised XX YY, ZZZZ; Accepted March 26, 2022)

Submitted to ApJ

ABSTRACT

We examine the robustness of the color-color selection of quiescent galaxies (QGs) against contamination of dusty star-forming galaxies using latest submillimeter data. We selected 18,304 QG candidates out to $z \sim 3$ using the commonly adopted $NUV-r-J$ selection based on the high-quality multi-wavelength COSMOS2015 catalog. Using extremely deep 450 and 850 μm catalogs from the latest JCMT SCUBA-2 Large Programs, S2COSMOS and STUDIES, as well as ALMA submillimeter, VLA 3 GHz, and *Spitzer* MIPS 24 μm catalogs, we identified luminous dusty star-forming galaxies among the QG candidates. We also conducted stacking analyses in the SCUBA-2 450 and 850 μm images to look for less-luminous dusty galaxies among the QG candidates. By cross-matching to the 24 μm and 3 GHz data, we were able to identify a sub-group of “IR-radio-bright” QGs who possess a strong 450 and 850 μm stacking signal. The potential contamination of these luminous and less-luminous dusty galaxies account for approximately 10% of the color-selected QG candidates. In addition, there exists a spatial correlation between the luminous star-forming galaxies and the QGs at a $\lesssim 60$ kpc scale. Finally, we found a high QG fraction among radio AGNs at $z < 1.5$. Our data show a strong correlation between QGs and radio AGNs, which may suggest a connection between the quenching process and the radio-mode AGN feedback.

Keywords: galaxies: evolution – galaxies: star formation – galaxies: statistics – galaxies: high-redshift
– submillimeter: galaxies

1. INTRODUCTION

Quiescent galaxies (QGs) are defined as galaxies with their star formation rates (SFR) lower than the average SFR of star-forming galaxies (SFGs) of similar stellar masses at similar redshifts (i.e., below the “main sequence”; Daddi et al. 2007; Elbaz et al. 2007; Noeske et al. 2007; Wuyts et al. 2011; Ciambur et al. 2013). The quenching mechanism of QGs is an important topic, especially for high-redshift ones. Observations showed that populations of massive QGs exist at $z \sim 1.0$ – 2.0 (Belli et al. 2017a; Carnall et al. 2019; Newman et al. 2018), and that half of the most massive QGs were formed at $z \sim 1.5$ (Ilbert et al. 2013; Muzzin et al. 2013). In recent studies, the QG population has been extended to $z \sim 4.0$ (Straatman et al. 2014; Glazebrook et al. 2017; Merlin et al. 2018; Schreiber et al. 2018b; Carnall et al. 2020; Forrest et al. 2020a,b; Valentino et al. 2020). Among these, Valentino et al. (2020) reported three QGs with stellar masses around $10^{11} M_{\odot}$ and with SFR ranging from 1.1 to $24.0 M_{\odot} \text{ year}^{-1}$ (1.0 to 2.1 σ below the main sequence) at $z = 3.775$, 4.012, and 3.767. How these high- z QGs can increase their mass and quench the star formation in a short period is still not fully understood.

Active galactic nucleus (AGN) feedback is one of the proposed scenarios to explain the rapid quenching (Bower et al. 2006; Croton et al. 2006; Somerville et al. 2008; Fabian 2012; Man & Belli 2018). AGN activities may either provide kinetic energy to the interstellar medium in the host galaxies and reduce the star formation efficiency, or heat up the gas to prevent the gas from cooling (radio mode AGN feedback; Croton et al. 2006; Bower et al. 2006; Fabian 2012; Somerville et al. 2008). AGN activities may also remove the gas and terminate the star formation (quasar mode AGN feedback; Fabian 2012; Somerville et al. 2008).

However, there are also other theoretical scenarios for the quenching mechanism. For example, the existence of turbulence may also provide kinetic energy to the system and result in morphological quenching (Martig et al. 2009; Dekel et al. 2009). Another example would be positive AGN feedback. In this case, AGN activities enhance star formation but rapidly consume the gas, resulting in a quenched galaxy (Ishibashi & Fabian 2012; Zhuang & Ho 2020; Shangguan et al. 2020). Other theoretical scenarios include mergers, stellar feedback, virial shock heating, etc (see discussion in Man & Belli 2018, and references therein), and the quenching of massive

galaxies could be a combination of some of these scenarios. Which of the mentioned scenarios is the dominant channel of the quenching mechanism remains unclear.

Here we would like to first focus on the foundation of the QG studies, the selection criteria of QGs. Rest-frame color-color diagrams are widely applied to selecting QGs. They are often composed of two rest-frame colors: a UV-to-optical color (typically as the y -axis) to distinguish blue SFGs from red QGs using the strong UV emission from young stars, and an optical-to-near-infrared color (typically as the x -axis) to distinguish old passive stellar populations from dusty/reddened young stellar populations. Such photometric selections are very convenient since only photometric data are needed. There are various kinds of color-color diagrams proposed for QG selections based on rest-frame absolute magnitudes, such as the U – V – J diagram (Wuyts et al. 2007; Williams et al. 2009; Muzzin et al. 2013), the NUV – r – J diagram (Ilbert et al. 2013), and the NUV – r – K diagram (Arnouts et al. 2013).

Despite the great success of using color-color diagrams to select large samples of QGs, there are potential issues in such selections. First, the selection boundary that separates QGs and SFGs in a color color diagram was decided empirically (e.g., Ilbert et al. 2013; Muzzin et al. 2013; Williams et al. 2009). Whether a set of selection criteria are still applicable to different datasets should be examined. Second, either because of the intrinsic properties of SFGs and QGs, or because of photometric errors, the distribution of the two groups of galaxies can have unknown levels of overlap around the selection boundaries. It was found that adjusting the position of the boundary by ± 0.1 mag could greatly change the selection efficiency and the subsequent analyses based on the selected samples (Muzzin et al. 2013, Appendix B therein).

One important factor here is that our understanding of dusty galaxies is limited. The spectral energy distribution (SED) of these high- z dusty galaxies may be more complicated than what was initially assumed to setup color selection. The selected QG “candidates” may still suffer from contamination by red dusty SFGs at high z . For instance, a $z = 3.717$ QG candidate (Straatman et al. 2014; Glazebrook et al. 2017) was detected at 450 and $870 \mu\text{m}$ (Simpson et al. 2017). This implies that the target is a dusty SFG, or is an interacting system consisting of a QG and a dusty galaxy (e.g., Schreiber et al. 2018b), or at least contains a significant dusty

star-forming component. Such contamination may lead to an overestimated number density of QGs, especially at high z , which may have consequences in our pursuit of an understanding of the quenching mechanism.

Therefore, in this paper, we would like to revisit the selection of QGs using color-color diagrams. We will examine the quiescence of our color-selected QG candidates using submillimeter observations. Various previous studies were carried out to analyze the star formation of color-selected QGs. Some studies measured the SFR by either applying SED fittings from the UV to mid-infrared bands (Fumagalli et al. 2014; Merlin et al. 2018; Carnall et al. 2019; Toba et al. 2019), using spectroscopic data (Schreiber et al. 2018c; Belli et al. 2017a), or measuring $H\alpha$ emission (Belli et al. 2017b). Others searched for far-infrared dust emissions using *Spitzer* observations (Fumagalli et al. 2014; Man et al. 2016; Gobat et al. 2018; Magdis et al. 2021), *Herschel* observations (Viero et al. 2013; Man et al. 2016; Straatman et al. 2014; Merlin et al. 2018; Gobat et al. 2018; Magdis et al. 2021) or Atacama Large Millimeter/submillimeter Array (ALMA) observations (Santini et al. 2019; Schreiber et al. 2018c; Simpson et al. 2017). Others also searched for gas content in QG candidates (Sargent et al. 2015; Young et al. 2011). In particular, Man et al. (2016) measured the dust emission of their color-selected QGs by stacking *Herschel* SPIRE data at 250, 350, and 500 μm (FWHM $\simeq 18''.2$, $24''.9$, and $36''.3$), and they claimed that contamination of dusty SFG is $\sim 15\%$ among their QG candidates. We will follow the approach in Man et al. (2016) but re-examine the issue with higher angular resolutions using JCMT SCUBA-2 450 and 850 μm data (FWHM = $7''.9$ and $13''$) and ALMA data.

In this study, we selected 18,304 QG candidates using the *NUV-r-J* diagram with deep galaxy samples from the COSMOS field (Laigle et al. 2016) and analyzed the properties of the selected QG candidates. In the first part of our study, we estimated the contamination of dusty SFGs among the QG candidates by cross-matching them to the multi-wavelength catalogs as well as performing stacking analyses in the submillimeter images. We also estimated the effect of chance projection in the cross-matching and estimated the degrees of small-scale clustering. In the second part of our study, we further investigated the AGN feedback as a potential quenching mechanism among QG candidates. We examined the relation between various AGNs and the QG candidates in our data by calculating the QG fractions in the AGN samples.

We describe our data in Section 2 and introduce the QG color-color selection in Section 3. In Sections 4 and 5, we analyze the contamination of dusty SFGs among

the *NUV-r-J* selected QG candidates. We also examine the small-scale clustering between dusty SFGs and QG candidates in Section 4.2. In Section 6, we discuss the QG fractions among our AGN samples. Section 7 gives a summary of our results. We use the Chabrier (2003) initial mass function (IMF) and an $H_0 = 70 \text{ km s}^{-1} \text{ Mpc}^{-1}$, $\Omega_\Lambda = 0.7$, and $\Omega_m = 0.3$ cosmology throughout this study.

2. MULTI-WAVELENGTH DATA

2.1. COSMOS2015 Catalog

We selected galaxies from the multi-wavelength band-merged COSMOS2015 catalog (Laigle et al. 2016). To use the rest-frame absolute magnitudes for our color selection, we excluded those labeled as failure in SED fitting to avoid bad absolute magnitudes. We also excluded samples that are labeled as stars. We excluded galaxies with extreme values in the catalog (*NUV*, *r*, and *J* absolute magnitudes that are < -30 or > 0 , and negative redshifts), which are likely caused by either catastrophic failures in SED fitting or problematic photometry. These selection criteria reject $\sim 57\%$ (677,085/1,182,108) of the initial sample.

We further limited the errors of the magnitudes in K_S band to be lower than 0.2. This uniform selection ensures that our sample has a robust set of photometry and avoids biasing against high- z sample. The limiting magnitude is 23.7 for K_S band. The selection criterion of the K_S band magnitude error further rejects $\sim 29\%$ (344,806/1,182,108) of the initial sample. Overall, the majority of the rejections are caused by their faintness. They either are not detected at K_S or have $K_S > 24$.

With the above selection criteria, we obtained a total sample size of 160,217 galaxies from the COSMOS2015 catalog. They all have high-quality SED fitting results; all of them have SED fitting based on at least nine filters, and 98% of them more than 28 filters. The sample covers an area of 1.58 deg^2 in the COSMOS field (Fig. 1). We used stellar mass M_* , photometric redshift z , and rest-frame absolute magnitudes M_{NUV} , M_r , and M_J from the COSMOS2015 catalog, which were derived from SED fittings. The sample has stellar masses up to $M_* = 10^{12} M_\odot$ and redshifts over $z \sim 4$ (Fig. 2 (b) and (c)). The absolute magnitudes will be applied for our QG selection in the next section.

2.2. Submillimeter Data

We used submillimeter data in the COSMOS field from JCMT SCUBA-2 (Holland et al. 2013, 1999) at 450 μm (STUDIES, Wang et al. 2017; final data release in Gao et al. 2021, in prep.) and 850 μm (S2COSMOS, Simpson et al. 2019), in order to search for dusty SFGs

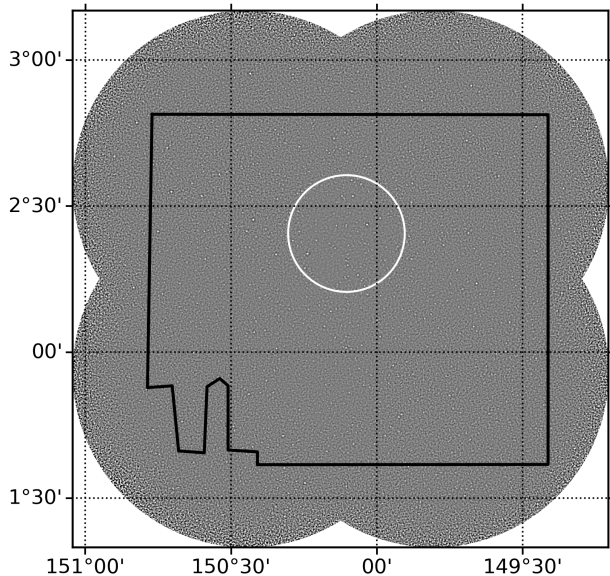


Figure 1. Coverage maps of the COSMOS field. The background shows the S2COSMOS 850 μm image. The black polygon corresponds to the coverage of our K_s band selected COSMOS2015 sample, while the white circle corresponds to the 151-arcmin² coverage of STUDIES 450 μm image. The MIPS 24 μm and VLA 3 GHz catalogs cover the whole area of the black polygon and are not shown in this figure.

that contaminate the QG sample. The 450 μm map covers the central 151 arcmin² of COSMOS, while the 850 μm map covers the whole COSMOS field (Fig. 1). The 450 μm and 850 μm maps have detection limits of about 3.5 mJy and 2 mJy, respectively. The detection limits are all substantially higher than the confusion noise ($\sigma_c \sim 0.7$ mJy at 450 μm , e.g., Lim et al. 2020; $\sigma_c \sim 0.5$ mJy at 850 μm , e.g., Simpson et al. 2019).

In total, we selected 357 objects with 450 μm detection and 1,147 objects with 850 μm detection from the SCUBA-2 maps. Four of the 450 μm sources and 166 of the 850 μm sources located outside the region occupied by our optically selected sample, because of the difference in area coverage and the masks in the COSMOS2015 catalog (Fig. 1). Among the remaining 353 objects with 450 μm detection and 981 objects with 850 μm detection, 77 and 370, respectively, have ALMA observations from the AS2COSMOS and A3COSMOS catalogs (Section 2.3).

Since the SCUBA-2 maps have relatively low angular resolution, we could not reliably identify the optical counterparts to the submillimeter sources. We therefore include the auxiliary data in section 2.3 for the process of cross matching COSMOS2015 galaxies to SCUBA-2 sources, and the details will be described in section 4.1.

2.3. Auxiliary Data

We included *Spitzer* MIPS 24 μm , VLA 3 GHz, and ALMA catalogs in our study for their better astrometry when our submillimeter data do not have sufficient angular resolution and for analyzing QG properties.

For 24 μm data, we used the *Spitzer* MIPS S-COSMOS image from Sanders et al. (2007). In order to generate a catalog deeper than the archival MIPS catalog of Sanders et al. (2007), 24 μm sources were extracted using SExtractor (Bertin & Arnouts 1996), and their fluxes were re-calibrated to their *Spitzer* General Observer Cycle 3 total fluxes. Our MIPS 24 μm catalog has a 3.5σ detection limit of 57 μJy , in contrast to the flux cut at 150 μJy in Sanders et al. (2007). Our catalog is very similar to the catalog of Le Floc’h et al. (2009) in terms of total numbers of detections. The fluxes are also consistent within 6% (Lim et al. 2020) as we calibrated our fluxes to that of Sanders et al. (2007).

We cross-matched the COSMOS2015 catalog with our MIPS 24 μm catalog using a search radius of 2'', which corresponds to about 1/3 of the beam size at 24 μm . 26,999 galaxies (16.9%) are matched to the MIPS 24 μm sources.

For 3 GHz data, we directly adopted the identification of the COSMOS2015 objects in the VLA catalog of Smolčić et al. (2017a), which used a search radius of 0''.8. The 5σ detection limit of the VLA catalog of Smolčić et al. (2017a) is 2.3 $\mu\text{Jy beam}^{-1}$. 6,002 galaxies (3.7%) are matched to the VLA 3-GHz sources.

We also used catalogs derived from ALMA observations, including the AS2COSMOS (Simpson et al. 2020) and A3COSMOS (Liu et al. 2019) catalogs. The AS2COSMOS catalog was derived from the follow-up 343 GHz observations of 186 bright 850 μm sources in the S2COSMOS catalog. The AS2COSMOS sources are essentially complete for the S2COSMOS sources above 6.2 mJy; only one S2COSMOS source does not have ALMA detection. The A3COSMOS catalog collects ALMA archival data in the COSMOS field, at wavelengths from 671 to 90.2 GHz. We cross-matched our optical sample with the ALMA catalogs using a search radius of 1''. This search radius should allow us to overcome the intrinsic offsets between starlight and submillimeter emission from dusty galaxies (e.g., 1σ offset of 0''.55 in Chen et al. 2015).

2.4. AGN Sample

We also examined the AGN properties of our sample. We cross-matched our sample with radio AGNs from the VLA catalog of Smolčić et al. (2017b), color-selected mid-IR AGNs from Chang et al. (2017), and X-ray AGNs selected from *Chandra* data by Civano et al. (2016) and Marchesi et al. (2016).

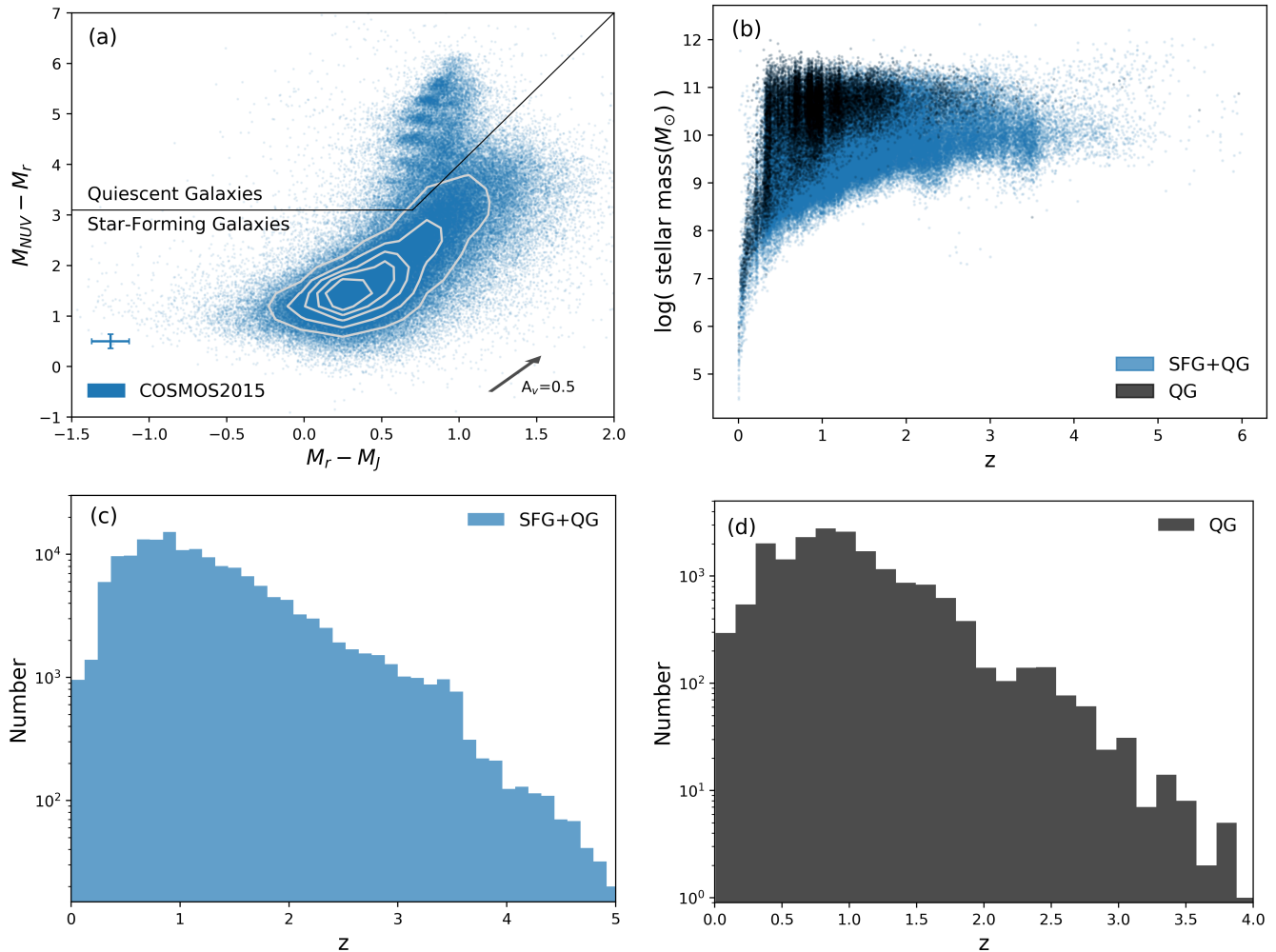


Figure 2. The full galaxy sample selected from the COSMOS2015 catalog. Panel (a) shows the distribution in the $NUV-r-J$ diagram, and the QG sub-sample is selected in upper-left corner. The fringe structure in the QG population may be caused by either the lack of QG template or by certain procedures in the SED fitting, but the structure does not affect our result. The reddening vector derived from Calzetti et al. (2000) extinction in the lower-right corner, while the typical (median) error in the two colors for all the sources is shown in the lower-left corner. Panel (b) and (c) show the stellar mass and the redshift distributions of the full galaxy sample (colored in blue), while panel (b) and (d) show those of the QG sub-sample (colored in black).

The radio AGNs were selected by comparing the observed radio emission to the expected radio emission from IR-derived SFR. Those exceeding 3σ in $\log(L_{1.4GHz}/SFR_{IR})$ are classified as radio AGNs (see the details in Smolčić et al. 2017b; Delvecchio et al. 2017). The mid-IR AGNs were selected in the rest-frame mid-IR color-color diagram. Those which exhibit red power-law SEDs in the mid-IR are classified as mid-IR AGNs (see the details in Chang et al. 2017; Lacy et al. 2004, 2007; Donley et al. 2012). The X-ray AGNs were selected with X-ray luminosity of $L_{X(2-10keV)} > 10^{42}$ ergs s^{-1} (Zezas et al. 1998; Ranalli et al. 2003; Szokoly et al. 2004). We note that if such an X-ray luminosity is produced purely by X-ray binaries rather than an AGN,

the inferred SFR would be $> 200 M_{\odot} \text{ yr}^{-1}$ using the conversion between SFR and L_X (e.g., Ranalli et al. 2003). Such a high SFR would be detected in our submillimeter analyses, but we do not observe it. Therefore, the majority of the $L_{X(2-10keV)} > 10^{42}$ ergs s^{-1} sources in our samples should be AGN-dominated.

3. COLOR-COLOR DIAGRAM

We applied the rest-frame $NUV-r-J$ color-color diagram to our sample in order to select QG candidates. Various color-color diagrams were used for QG selection, including the $U-V-J$ diagram (Williams et al. 2009) and the $NUV-r-J$ diagram (Ilbert et al. 2013). Although the $U-V-J$ diagram is more widely used than the $NUV-r-J$ diagram, there are advantages of using NUV and

r bands instead of U and V bands (Ilbert et al. 2013). The NUV band is at a shorter wavelength, so it is more sensitive to emission from young stars and extinction. The $NUV - r$ color has a wider wavelength span than the $U - V$ color, so it is less vulnerable to photometric errors. The rest-frame NUV band can be obtained from optical data toward higher redshifts, around $z > 2$, where U band starts to enter the near-IR. This leads to better sensitivities. Because of the above, we adopted the $NUV-r-J$ diagram in this study. We note that the selection results of using the two color-color diagrams are similar to each other. About 85% of our $NUV-r-J$ selected QG candidates overlap with the $U-V-J$ selected QG candidates, and the overlapping fraction slightly varies with redshift and the position of the selection boundary.

On the $NUV-r-J$ color-color diagram (Fig. 2 (a)), a blue color in y -axis indicates the starlight from young stars, while the color in x -axis breaks the degeneracy between age and dust reddening. QGs tend to locate in the upper-left corner of the diagram. We adopted the criteria proposed by Ilbert et al. (2013):

$$M_{NUV} - M_r > 3(M_r - M_J) + 1,$$

$$M_{NUV} - M_r > 3.1.$$

We selected 18,304 galaxies to be our QG candidates, which are 11.4 ± 0.1 % of the total (Fig. 2(a)). The selected QG candidates have a redshift distribution peaking at $z \sim 1.0$ and extending to ~ 3.0 (Fig. 2 (d)). Our selection result is well consistent with the flag “CLASS=0” in the COSMOS2015 catalog (Laigle et al. 2016), which applied the same $NUV-r-J$ selection method. Among the $24 \mu\text{m}$ detected galaxies, 5.9 ± 0.1 % enter the QG selection region and therefore are QG candidates (Fig. 3 (a)). Among the 3 GHz detected galaxies, 17.8 ± 0.5 % are QG candidates (Fig. 3 (b)). The redshift distributions of the $24 \mu\text{m}$ and 3 GHz detected QGs also peak at $z \sim 1.0$ but have larger fraction of QGs at high z (Fig. 3 (c)). The QG selection of submillimeter-detected galaxies will be described in Section 4.1. The numbers of selected QG candidates are summarized in Table 1.

To better understand the diagrams, we show the reddening vector and the typical (median) errors of the two colors in Fig. 2 (a), Fig. 3 (a), and Fig. 3 (b). The reddening vector is derived from Calzetti et al. (2000) extinction. For the magnitude errors, unfortunately the COSMOS2015 catalog does not provide errors in the absolute magnitudes. To have a rough idea of the errors, we followed the COSMOS2015 procedure (O. Ilbert & I. Davidzon, private communication) to select the nearest broad-band filter in the rest-frame that has a pho-

tometric error of < 0.3 . And we use the photometric error of that filter band as the absolute magnitude error. This clearly does not account for the errors in the K -corrections derived from the fitted SEDs, nor the errors propagated from the photo- z errors, but should still include a substantial part of the error budget.

With the above-estimated photometric errors, we could further estimate the fraction among the QG candidates that may originate from the SFG color space and scattered into the QG color space by the photometric errors. For each QG candidate, we generated 1,000 randomly perturbed NUV , r , and J band absolute magnitudes that follow Gaussian distributions according to the photometric errors. We then calculated the percentage of the perturbed colors that are located in the SFG region, i.e., the probability of the QG candidate to be selected as a SFG if there were no photometric errors. The average probability among our QG candidates is $\sim 7.5\%$, meaning that $\sim 7.5\%$ of our selected QG may have moved from the SFG color space across the boundary into the QG color space due to their photometric errors. The probabilities can help to understand the nature of dusty SFG contamination in the color-selected QG population. We will further discuss this in Sections 4 and 5.

From Fig. 3 (a), we can see that most of the $24 \mu\text{m}$ detected QG candidates tend to distribute close to the selection boundary in the diagram. They can be either dusty galaxies entering the QG color space because of atypical SED shapes, simply regular SFGs scattered into the QG color space because of photometric errors (cross in Fig. 3 (a)), or chance projections in the cross matching. By measuring the search area of matching through $2''$ search radius, we estimated that 382 ± 20 out of the 1596 matches ($23.9 \pm 1.2\%$) can be chance projections. In Table 1, $24 \mu\text{m}$ detected galaxies have lower QG fractions than that of all the COSMOS2015 sample. $24 \mu\text{m}$ sources are sensitive to dust emission, and the low fraction suggests a low dusty-galaxy contamination in the QG color selection.

On the other hand, the 3 GHz detected QG candidates distribute well into the QG selection region in Fig. 3 (b). If we calculate their vertical distances to the selection boundary, we obtain median values of 0.4 and 0.7 for the $24 \mu\text{m}$ and 3 GHz detected QG candidates, respectively. The median distance for the 3 GHz detected QGs is much larger than the typical photometric error (cross in Fig. 3 (b)), so they are not SFGs scattered into the QG color space. A large fraction of them should be real QGs harboring radio AGNs (see Section 6 and Fig. 8 for further evidence). In Table 1, the QG fraction among them is considerably higher than those of all the other

Table 1. Sample sizes and results of multi-wavelength cross-matching.

	SFGs+QGs	QGs	QGs/(all SFGs+QGs)	QGs/(all QGs)	QGs by chance projection
total in the COSMOS field	160217	18304	11.4±0.1 %	100 %	-
24 μm detected	26999	1596	5.9±0.1 %	8.72±0.22 %	382
3 GHz detected	6002	1066	17.8±0.5 %	5.82±0.18 %	-
850 μm detected	653	30	4.6±0.8 %	0.16±0.03 %	7.0
850 μm + ALMA	289	11	3.8±1.1 %	-	1.3
850 μm + 24 μm + 3 GHz	364	19	5.2±1.2 %	-	5.8
total in the STUDIES field	15296	1846	12.1±0.3 %	100 %	-
450 μm detected	239	8	3.3±1.2 %	0.43±0.15 %	2.5
450 μm + ALMA	58	2	3.4±2.4 %	-	0.3
450 μm + 24 μm + 3 GHz	181	6	3.3±1.4 %	-	2.1
radio AGN	1378	563	40.9±1.7 %	3.08±0.13 %	-
mid-IR AGN	791	95	12.0±1.2 %	0.52±0.05 %	-
X-ray AGN	2267	413	18.2±0.9 %	2.26±0.11 %	-

NOTE—The errors are set to be Poissonian, and only reflect the uncertainties caused by the finite sample sizes. The 850 μm and 450 μm detected samples are determined through both the low-resolution SCUBA-2 data and the high resolution auxiliary data. The auxiliary data are either ALMA data, or 24 μm and 3 GHz data (see Section 4.1 for details).

subgroups. This gives us a hint about the correlation between radio AGN and QG candidates, which will be discussed in Section 6.

4. BRIGHT SUBMILLIMETER GALAXIES AMONG QG CANDIDATES

In this section, we conduct a thorough analysis on the contamination of bright submillimeter galaxies among our QG candidates. In Section 4.1, we cross-matched our sample with the SCUBA-2 450 μm and 850 μm catalogs using the positions of MIPS 24 μm , VLA 3 GHz, and ALMA submillimeter sources. In Section 4.2, we further performed a blind cross-matching and reported the finding of small-scale clustering between QG candidates and SCUBA-2 sources.

4.1. Traditional Cross Matching

4.1.1. Counterpart Identification using Auxiliary Data

We have searched for MIPS 24 μm , VLA 3 GHz, and ALMA counterparts in the COSMOS2015 catalog with data presented in Section 2.3. We can therefore search for the optical counterparts to the low-resolution SCUBA-2 submillimeter sources by including the high-resolution multi-wavelength information. Such a two-step counterpart identification method is traditionally used on SCUBA-2 sources. In general, this method was shown to be able to pick up some 2/3 of SCUBA-2 source counterparts (e.g., Casey et al. 2013; Koprowski et al. 2016; Cowie et al. 2017; Michałowski et al. 2017; An et al. 2018; Simpson et al. 2020; Lim et al. 2020), but

the exact fractions depend on the sensitivity of the high-resolution observations in the mid-IR, submillimeter, or radio.

We first cross-matched our optical sample with the SCUBA-2 450 μm and 850 μm sources using a search radius of 4'' and 7'', respectively. The search radii are approximately half of the full width at half maximum of the beams (FWHM = 7''.9 at 450 μm and 13'' at 850 μm). Such larger search radii (cf. 1/3 FWHM for the 24 μm matching) are required as the SCUBA-2 positional accuracy is more impacted by confusion effects and telescope pointing errors, rather than just the beam sizes. Then, from the matched sample, we narrowed down the optical counterparts by searching for ALMA detected galaxies from the AS2COSMOS and A3COSMOS catalogs (described in Section 2.3). For the remaining sources without ALMA detection, we identified their optical counterparts by searching for 24 μm and 3 GHz detected galaxies (described in Section 2.3). Those without MIPS and VLA counterparts are likely to be at higher redshifts ($z \gtrsim 3$, see Section 3.3 in Lim et al. 2020) and are not the main targets of interest in this paper given the redshift distributions in Fig. 2. We note that when there are multiple sources within the search radius, we consider all of the sources and narrow down the possible counterparts only with multi-wavelength information without considering their distances to the SCUBA-2 position.

The results of the cross-matching are summarized in Table 1. For the SCUBA-2 450 μm sources, we matched 58 COSMOS2015 galaxies through ALMA observations

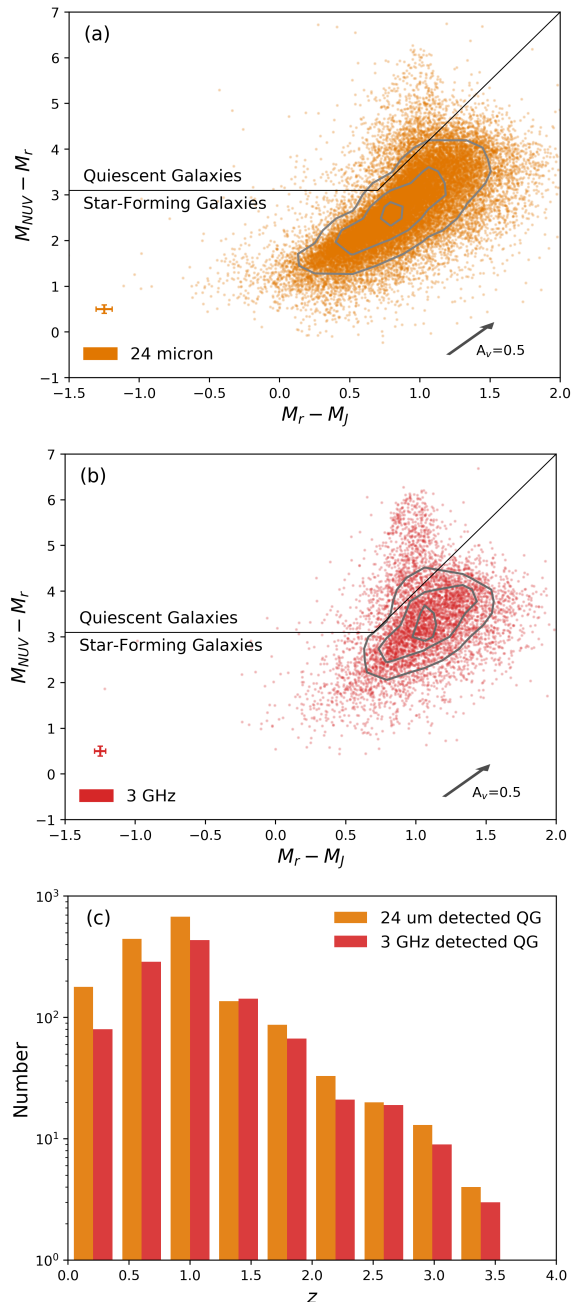


Figure 3. Distribution of the 24- μm detected sample (a) and the 3-GHz detected sample (b) in the $NUV-r-J$ diagram. The reddening vector derived from Calzetti et al. (2000) extinction and the typical errors in the two colors are also shown, as in Fig. 2 (a). The typical errors are smaller than that of the full galaxy sample (Fig. 2(a)). This is resulted from the higher fractions of bright galaxies among the two subgroups (median $r \sim 0.5$ magnitudes brighter).

The QG candidates are selected in upper-left corner of the panels, and the redshift distribution of the two QG subgroups are shown in (c). We note that the two subgroups have partial overlap between each other.

and 181 through the MIPS and VLA catalogs. We defined them as 450 μm detected galaxies. Two out of the 58 galaxies and six out of the 181 galaxies are selected as QG candidates in the $NUV-r-J$ diagram (Fig. 4 (a)). For the SCUBA-2 850 μm sources, there are 289 and 364 matches when using the ALMA catalogs and using the MIPS and VLA catalogs. We defined them as 850 μm detected galaxies. 11 out of the 289 galaxies and 19 out of the 364 galaxies are selected as QG candidates in the $NUV-r-J$ diagram (Fig. 4 (b)).

One thing worth noting is the distribution of 450 μm and 850 μm detected QG candidates in the $NUV-r-J$ diagrams in Fig. 4. Although the sample sizes are small here, these QG candidates do not appear to have a tendency of locating near the selection boundaries (cf. the 24 μm case in Fig. 3 (a)), comparing to the typical color errors (crosses in Fig. 4). This suggests that most of them are systems that consist of a quiescent component that dominates the rest-frame UV/optical emission and a dusty component that shows up in the far-IR. This can be either an interacting system like the one in Simpson et al. (2017) and Schreiber et al. (2018b), or a foreground quiescent galaxy which lenses a background dusty galaxy. Indeed, one of the QG candidate is matched to both 450 and 850 μm sources through ALMA observations. This target is likely to be a lensed system (star symbol in Fig. 4), and we will further discuss it in the end of this section and in Appendix A.

From the numbers of QG candidates that have 450 or 850 μm detections, we could estimate the fraction of the bright submillimeter galaxies among our QG candidates. The results show that $0.43 \pm 0.15\%$ (8/1,846) and $0.16 \pm 0.03\%$ (30/18,304) of our QG candidates are bright 450 μm and 850 μm sources, respectively (Table 1). The fraction of 450 μm detected QGs is slightly ($\sim 1.8\sigma$) larger than that of 850 μm ones. This may be a result of either the better luminosity sensitivity or the higher source density at 450 μm . The former allows us to detect more QGs at 450 μm , while the latter increases the probability of chance projection between unrelated QGs and 450 μm sources. If we remove the expected number of chance projections (Section 4.1.2), then the difference reduces to $\sim 1.3\sigma$. So the reason of the difference between the fractions at 450 and 850 μm remains unclear under our sample sizes.

We further split the populations into redshift bins (Table 2 and Fig. 5). We can see that the fraction of 850 μm detected QG candidates increases with redshift and rises up to $3.51 \pm 2.48\%$ at $z > 2$. This higher contamination rate at $z > 2$ could come from either a real redshift evolution, or simply larger photometric uncertainties on high-redshift sources. Nevertheless, this few-

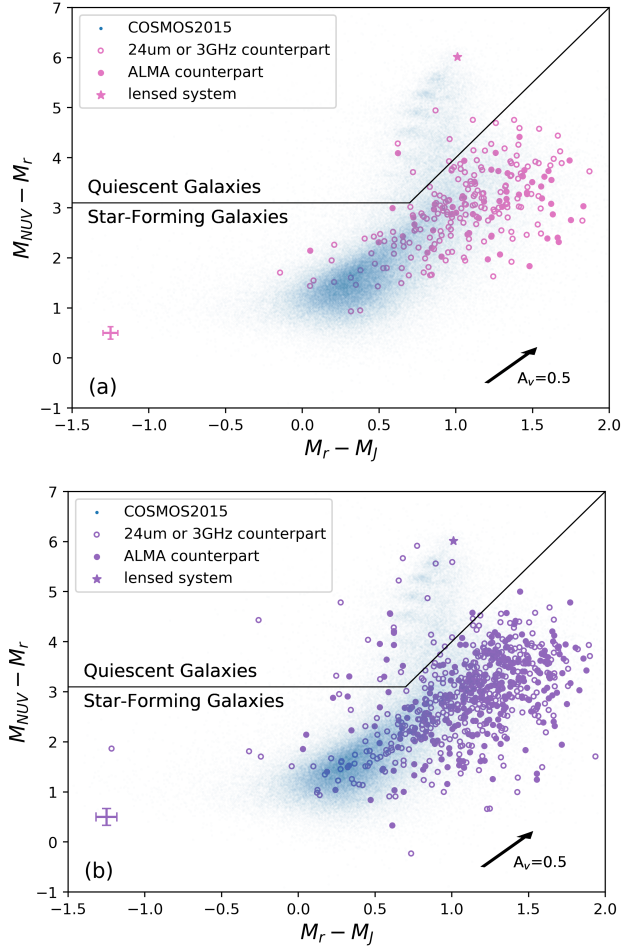


Figure 4. Distributions of the $450 \mu\text{m}$ (a) and $850 \mu\text{m}$ (b) detected sample in the $NUV-r-J$ diagram. The filled circles are samples matched to ALMA sources, while the empty circles are samples matched to $24 \mu\text{m}$ or 3 GHz sources. The star symbols show the position of the lensed system described in Appendix A. The reddening vector derived from Calzetti et al. (2000) extinction and the typical errors in the two colors for the submillimeter sources are also shown with arrows and crosses, respectively. The color errors of the $850 \mu\text{m}$ sources are larger because these sources are generally fainter in the optical than $450 \mu\text{m}$ sources.

percent contamination rate is still quite low. In conclusion, our QG candidates could be contaminated by bright dusty SFGs at a 0.16% to 0.43% level, and the contamination rises up to $\sim 1.7\%$ to 3.5% at higher redshift. We note that the contamination rates may be underestimated since we may not pick up all SCUBA-2 source counterparts in the two-step counterpart identification. We will perform a “blind” cross-matching in Section 4.2 to provide a different estimate of the contamination.

We analyze the role of photometric errors in the bright SMG contamination. In Section 3, we estimated the

probability of intrinsically being in the SFG color space but scattered into the QG color space by photometric errors for each QG candidate. The mean probabilities are 9.6% and 6.2% for $450 \mu\text{m}$ and $850 \mu\text{m}$ detected QGs, respectively. These both account for less than 10% of the SMG contaminations. Therefore, the bright SMG contamination is mainly due to intrinsic properties of the QGs rather than photometric errors.

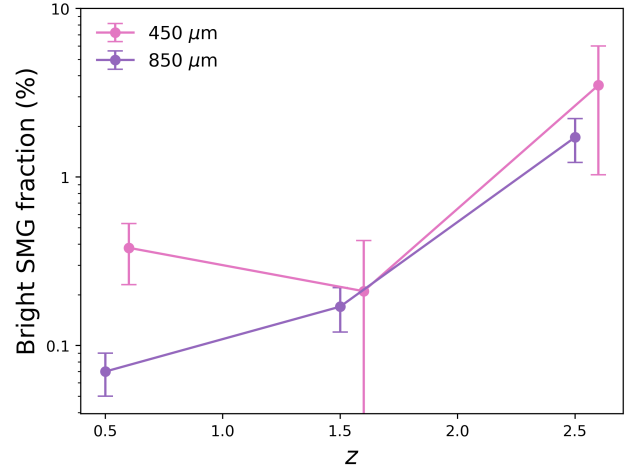


Figure 5. Percentage of bright submillimeter galaxies ($450 \mu\text{m}$ and $850 \mu\text{m}$ detected QGs) among COSMOS2015 QGs (Table 2) in logarithmic scale. The data points of $450 \mu\text{m}$ detected QGs are slightly offset along x -axis for clarity. The error bars of the $450 \mu\text{m}$ detected QGs are larger because of the smaller coverage of the STUDIES map. The errors are Poissonian.

In the above, we used both the AS2COSMOS and the A3COSMOS catalogs during the cross-matching. We can also estimate the contamination by matching QG candidates to only the AS2COSMOS catalog, which contains a homogeneous selection and complete observations of SCUBA-2 $850 \mu\text{m}$ sources with $S_{850\mu\text{m}} > 6.2 \text{ mJy}$ in the S2COSMOS map. If we match our QG candidates to $850 \mu\text{m}$ sources through only the AS2COSMOS catalog, we found 7 galaxies to be $850 \mu\text{m}$ detected QG candidates. If we assume the same QG fraction for all SCUBA-2 $850 \mu\text{m}$ sources, we estimate that there should be 36.9 ± 14.0 QG candidates. This accounts for $0.2 \pm 0.1\%$ among all the QG candidates. This agrees with the $0.16 \pm 0.03\%$ contamination mentioned above.

Furthermore, the SCUBA-2 catalog has a detection limit of 2 mJy but is not complete for sources above 2 mJy . The complete number of $850 \mu\text{m}$ sources can be estimated from the sources counts corrected for completeness, from Simpson et al. (2019). If we estimate the complete number of sources above 2 mJy and assume the same QG fraction in the AS2COSMOS catalog, we

Table 2. Percentage of bright submillimeter galaxies (sub-mm detected QGs) among COSMOS2015 QGs.

	total in the	850 μm detected	percentage	total in the	450 μm detected	percentage
	COSMOS field			STUDIES field		
all	18304	30	$0.16\pm 0.03\%$	1846	8	$0.43\pm 0.15\%$
$z \leq 1$	11562	8	$0.07\pm 0.02\%$	1314	5	$0.38\pm 0.17\%$
$1 < z \leq 2$	6045	10	$0.17\pm 0.05\%$	475	1	$0.21\pm 0.21\%$
$z > 2$	697	12	$1.72\pm 0.50\%$	57	2	$3.51\pm 2.48\%$

NOTE—The errors are set to be Poissonian. The 850 μm and 450 μm detected samples are determined through both the low-resolution SCUBA-2 data and the high resolution auxiliary data.

obtain a dusty galaxy contamination rate of $0.6\pm 0.3\%$. The relative uncertainty here is slightly larger than that simply propagated from the number of QGs in the AS2COSMOS catalog since the source counts also contain an uncertainty. Nevertheless, this value is larger than the above-estimated value of $0.16\pm 0.03\%$ and is probably a more realistic estimate if we do have a deeper and more complete survey at 850 μm .

We note that one out of the 11 QG candidates (ID = 659416 in the COSMOS2015 catalog) that are matched to SCUBA-2 850 μm sources through ALMA catalogs is likely to be a lensed system because of its unusual submillimeter/radio flux ratio (see Appendix A for details). This example demonstrates that when matching QG candidates to the submillimeter sources, a match does not imply the QG candidate and the long-wavelength source to be the same object. They could be physical associations such as the lensed system here, or an interacting galaxy pair consisting of a QG and a dusty object (e.g., Schreiber et al. 2018b). Based on our small sample size, the probability for such association is about 9% (1/11). Such spatial correlation effects caused by lensing or galaxy interaction will be further discussed in Section 4.2.

4.1.2. Effect of Chance Projection

Given the small numbers of matched objects in the previous section, we would like to examine whether the matches between our QG candidates and bright submillimeter sources are caused by chance projection or by real spatial correlation. We could estimate the effect of chance projection by simple calculations.

First, we calculated the search area in our 2-step cross matching. For the SCUBA-2 sources with ALMA observation, we used a search radius of $1''$ for the ALMA sources. For the remaining ones, we used search radii of $2''$ and $0.8''$ for 24 μm and 3 GHz sources, respectively. If a 3 GHz source located within the $2''$ search radius of a 24 μm source, we only adapted the search area of the

3 GHz source. We then calculated the expected fraction of randomly distributed QG candidates locating in the search area with $1 - e^{-na/A}$, where A is the survey area, n is the number of searched sources in the high-resolution catalogs, and a is the search area per source. The estimated numbers of chance projections are given in the last column of Table 1. When we matched through ALMA catalogs, the numbers of chance projections is significantly lower. When we matched through 24 μm and 3GHz catalogs, the probability of chance projections is about 1/3; 2.1 out of 6 (35.0%) and 5.8 out of 19 (30.5%) matches can be chance projections for 450 and 850 μm detected QG candidates.

We conclude that among the submillimeter detected QG candidates mentioned in the previous section, accounting for 0.16% to 0.43% among our QG candidates, the majority are real physical associations. The estimated bright dusty SFG contamination is not mainly driven by chance projections.

4.2. Blind Cross-Matching

4.2.1. Matching with Large Radii and Estimate of Chance Projection

In the cross-matching aided by 3 GHz and 24 μm astrometry described in Section 4.1, there is a possibility that the real optical counterparts of the submillimeter sources are undetected at 3 GHz and/or 24 μm . The different redshift dependences of sensitivities in the submillimeter, radio, and mid-IR may introduce such a bias. To avoid this, we can perform a “blind” cross-matching to the SCUBA-2 sources. We directly match the QG candidates with SCUBA-2 450 μm and 850 μm sources using $4''$ and $7''$ search radii, respectively, without relying on radio and mid-IR positions. The large matching radii here will unavoidably lead to larger numbers of chance projections, so we need to more precisely estimate the number of chance projections.

To do this, we simulated the matching results using SCUBA-2 submillimeter sources with random positions.

Here we do not apply the $1 - e^{-na/A}$ method because the distribution of QGs may not be random at the scale of the relatively large search radii for SCUBA-2 sources and therefore the dispersion in the mean cannot be estimated. We calculated the expected number of QG candidates located within a search radius from the randomly distributed submillimeter sources and compared the results with the actual number of matched QG candidates. The simulation is repeated 1,000 times. The estimated number of matches and its error are set to be the mean and the 68% interval of the 1,000 results. The results are summarized in Table 3, and the fractional difference between the expected matches (chance projections) and the actual matches are also shown in Fig. 6. We note that the detection limit of the SCUBA-2 450 μm , 850 μm , and ALMA sources are different. We also estimated the probability that the expected number is equal to or larger than the actual number (Table 3). We show the results of SFGs for comparison in Table 4.

The first and fifth rows of Table 3 and 4 presents simple cross-matching between the QGs/SFGs and single-dish submillimeter samples without information from ALMA. For SCUBA-2 450 μm sources, the actual matches are $42.6^{+22.9}_{-21.3}\%$ larger than the expected random matches. Although the significance is only about 2σ (Fig. 6 (a)), the estimated probability that the expected number equals to or is larger than the actual number is 0.05, which is quite low. This result suggests that there are $8.7^{+4.7}_{-4.3}$ QGs physically associated with the 353 450 μm sources. This corresponds to $0.47^{+0.25}_{-0.23}\%$ of the 1846 QGs in the 450 μm map area. The statistically derived number of $8.7^{+4.7}_{-4.3}$ matches also nicely agrees with the 8 matches found with high-resolution data (Section 4.1 and Table 1). Also, for comparison, $316.3^{+12.3}_{-12.7}$ SFGs are physically associated with the 353 450 μm sources. This is as expected, since dusty submillimeter sources should be dominated by SFGs.

For SCUBA-2 850 μm sources, the actual matches are $52.6^{+8.9}_{-8.9}\%$ larger than the expected random matches (see also 6 (b)), which is significant ($\sim 6\sigma$). The estimated probability that the expected number equals to or is larger than the actual number is nearly zero. This means that among the 206 matches between the QGs and 850 μm sources, 71 ± 12 are real physical associations. These ~ 71 sources account for $0.39 \pm 0.07\%$ of the 18304 QGs. We note that the number of 71 is significantly different from the number of 30 quoted in Table 1, or 23 after removing the expected number of chance projections. This is because here we do not require high-resolution multi-wavelength data to pin down the cross-matching. This suggests that a significant fraction of QG–850 μm associations in our data do not have 24 μm , 3 GHz, or

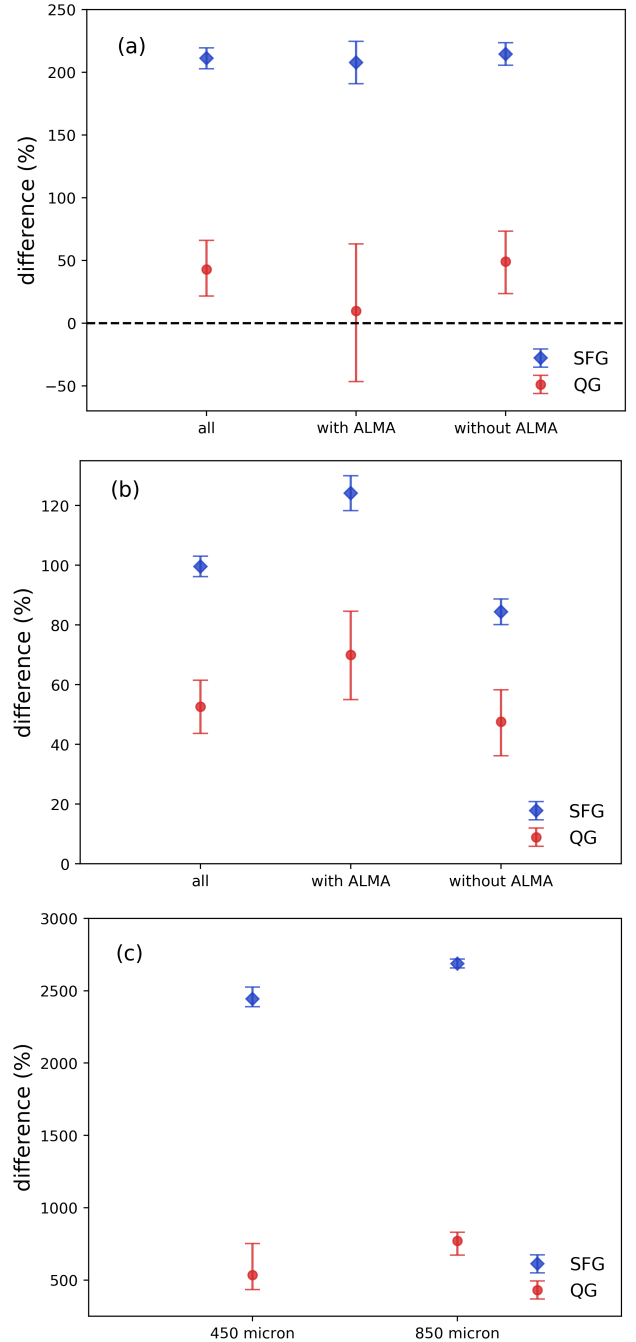


Figure 6. Fractional differences between the actual matches and the expected matches based on random spatial distributions (see also Table 3). Panels (a), (b), and (c) show results for SCUBA-2 450 μm , 850 μm , and ALMA sources, where $4''$, $7''$, and $1''$ search radii are used respectively. It can be seen that the QG results for the SCUBA-2 850 μm sources and ALMA sources are all significantly above zero, showing that these extra matches in the actual sample are caused by real physical connection between the QG candidates and the submillimeter sources, rather than chance projection.

ALMA counterparts. This is perhaps partially because

Table 3. Cross-Matches and Expected Chance Projections between QGs and Submillimeter Sources

SCUBA-2 sources	Group	Match Radius ^a	Number	Expected Matched QG	Actual Matched QG	Difference	Fractional Difference	Probability ^b
450 μm sources	all	4''	353	20.3 ^{+4.7} _{-4.3}	29	8.7 ^{+4.7} _{-4.3}	42.6 ^{+22.9} _{-21.3} %	0.05
	without ALMA	4''	276	16.1 ^{+3.9} _{-4.1}	24	7.9 ^{+3.9} _{-4.1}	48.9 ^{+24.1} _{-25.5} %	0.046
	with ALMA	4''	77	4.6 ^{+2.4} _{-2.6}	5	0.4 ^{+2.4} _{-2.6}	9.6 ^{+53.5} _{-56.1} %	0.475
	ALMA sources	1''	85	0.3 ^{+0.7} _{-0.3}	2	1.7 ^{+0.7} _{-0.3}	534.9 ^{+217.5} _{-100.0} %	0.042
850 μm sources	all	7''	981	135.0 ^{+12.0} _{-12.0}	206	71.0 ^{+12.0} _{-12.0}	52.6 ^{+8.9} _{-8.9} %	0
	without ALMA	7''	611	84.6 ^{+10.4} _{-9.6}	120	35.4 ^{+10.4} _{-9.6}	41.8 ^{+12.2} _{-11.4} %	0
	with ALMA	7''	370	50.6 ^{+7.4} _{-7.6}	86	35.4 ^{+7.4} _{-7.6}	69.8 ^{+14.5} _{-15.1} %	0
	ALMA sources	1''	452	1.3 ^{+0.7} _{-1.3}	11	9.7 ^{+0.7} _{-1.3}	771.6 ^{+58.5} _{-100.0} %	0

^aThe radius of 1'' to 7'' correspond to 8–56 kpc at $z = 1$ and 8–57 kpc at $z = 2.5$.

^bThe probability that the expected number of matches (based on random spatial distribution) is equal to or larger than that of the actual matches.

Table 4. Cross-Matches and Expected Chance Projections between SFGs and Submillimeter Sources

SCUBA-2 sources	Group	Match Radius ^a	Number	Expected Matched SFG	Actual Matched SFG	Difference	Fractional Difference	Probability ^b
450 μm sources	all	4''	353	149.7 ^{+12.3} _{-12.7}	466	316.3 ^{+12.3} _{-12.7}	211.3 ^{+8.2} _{-8.5} %	0
	without ALMA	4''	276	116.4 ^{+10.6} _{-10.4}	366	249.6 ^{+10.6} _{-10.4}	214.3 ^{+9.1} _{-9.0} %	0
	with ALMA	4''	77	32.5 ^{+5.5} _{-5.5}	100	67.5 ^{+5.5} _{-5.5}	207.6 ^{+16.9} _{-16.9} %	0
	ALMA sources	1''	85	2.2 ^{+1.8} _{-1.2}	56	53.8 ^{+1.8} _{-1.2}	2443.1 ^{+81.7} _{-54.6} %	0
850 μm sources	all	7''	981	1045.7 ^{+35.5} _{-35.9}	2087	1041.3 ^{+35.5} _{-35.9}	99.6 ^{+3.4} _{-3.4} %	0
	without ALMA	7''	611	652.9 ^{+28.1} _{-27.9}	1204	551.1 ^{+28.1} _{-27.9}	84.4 ^{+4.3} _{-4.3} %	0
	with ALMA	7''	370	394.0 ^{+23.0} _{-23.0}	883	489.0 ^{+23.0} _{-23.0}	124.1 ^{+5.8} _{-5.8} %	0
	ALMA sources	1''	452	9.9 ^{+3.1} _{-2.9}	277	267.1 ^{+3.1} _{-2.9}	2687.3 ^{+30.8} _{-29.6} %	0

^{ab}The parameters follow those in Table 3.

of the insufficient sensitivity (24 μm and 3 GHz cases) and incomplete coverage (ALMA cases). However, we will soon show that a large fraction of these 71 sources are clustered around the SCUBA-2 sources at a $\sim 7''$ scale, but they are not the submillimeter, mid-IR, or radio emitters. Finally, as in the case for 450 μm cross-matching, the overlap between 850 μm sources and SFGs is much larger than that for QG, which is expected.

4.2.2. Verification and Comparison with ALMA Sources

The above “blind” matching between QG candidates and SCUBA-2 sources using large matching radii (1/2 of the single-dish beam FWHM) and the comparison between actual matches and simulations allows us to statistically assess the numbers of real physical associations. Now with the ALMA data, we can pin down the cross-

matching with a much smaller matching radius, with a smaller subsample. We split the SCUBA-2 sources into those with and without ALMA observations. The results are listed in the remaining rows of Table 3 and 4.

As a simple sanity check, we ran cross-matching with large matching radii over the subsamples. The fractional differences between actual and expected random matches do not change significantly between the ALMA and non-ALMA subsamples for QGs (Fig. 6 (a) and (b)). This is even true for the 450 μm sample, albeit the small sample sizes and therefore the large errors. This implies that there is no special selection bias in the ALMA observations regarding their QG-submillimeter properties.

For the SCUBA-2 sources with ALMA observations, the expected numbers for matches under a $1''$ search radius and random spatial distributions are always small comparing to the actual matches. This is reflected on the large fractional differences between the actual matches and expected random matches, which are $534.9_{-100.0}^{+217.5}\%$ for the $450\ \mu\text{m}$ sources and $771.6_{-100.0}^{+58.5}\%$ for the $850\ \mu\text{m}$ sources (Fig. 6(c), the fourth and eighth rows). This means that the majority of the observed matches between QGs and ALMA sources under a $1''$ matching radius are real physical associations.

An interesting comparison is to see if the $1''$ matching pinned down by ALMA agrees with the statistical estimates of real physical associations derived from the large-radius blind matching. Table 3 and 4 show that if we match the 77 SCUBA-2 $450\ \mu\text{m}$ sources to QGs and SFGs using a $4''$ matching radius, we expect $0.4_{-2.6}^{+2.4}$ out of the 5 QG matches and $67.5_{-5.5}^{+5.5}$ out of the 100 SFG matches to be real associations. These can be compared with the ALMA results for the same sub-sample: $1.7_{-0.3}^{+0.7}$ and $53.8_{-1.2}^{+1.8}$ real associations for the QGs and the SFGs. The values for QG–SMG associations agree nicely, albeit the small sample size. This probably validates the statistical method for estimating the number of real associations and chance projections using simulations and random distributions. On the other hand, the values for SFG–SMG associations (67.5 and 53.8) differ by 25% and the difference is about 2σ . The excess in the number of SFGs around SMGs within $4''$ comparing to the number of true associations pinpointed by ALMA suggests a weak clustering of SFGs around SMGs. This excess is only 2σ and is not statistically significant. However, if we look at the $850\ \mu\text{m}$ values, the excesses for both QG–SMG and SFG–SMG associations become highly significant.

We make a similar comparison on the $850\ \mu\text{m}$ ALMA subsample. The expected numbers of real associations under a $7''$ matching radius for the 370 $850\ \mu\text{m}$ sources are $35.4_{-7.6}^{+7.4}$ and $489.0_{-23.0}^{+23.0}$ for QGs and SFGs, respectively. However, the numbers revealed by ALMA observations are much smaller: $9.7_{-1.3}^{+0.7}$ and $267.1_{-2.9}^{+3.1}$. The differences between the two sets of numbers are both significant. This implies that once we increase the matching radius from $1''$ to $7''$ ($\lesssim 60\ \text{kpc}$ at $z = 1-2$), additional clustering effects kick in, i.e., there are QGs and SFGs physically associated with the submillimeter sources at such large scales, but they are not the submillimeter sources themselves nor arcsec-scale galaxy-galaxy lensing pairs. This effect becomes undetectable (QGs) or much weaker (SFGs) under the $4''$ matching for the $450\ \mu\text{m}$ sources, either because of the small sample

sizes for the $450\ \mu\text{m}$ analysis or because of the different spatial distribution for low-dust-luminosity sources.

Previous studies of QG autocorrelation functions found that QGs show stronger clustering signal than SFGs at arcminute scales (Williams et al. 2009), but there do not exist QG–SFG or QG–SMG cross-correlation analyses. Our results suggest that QGs and SMGs are clustered, and detailed cross-correlation studies between these two distinct populations will be an interesting future topic.

In summary, with direct cross-matching to SCUBA-2 sources and statistical analyses of chance projection effects, we do not find evidence for a different dusty galaxy contamination rate among QGs comparing to what we found with counterpart identifications using ALMA, $24\ \mu\text{m}$, and 3 GHz data. Instead, we found a clustering effect between the bright submillimeter sources and our QG candidates at scales from $1''$ to $7''$ ($\sim 8-60\ \text{kpc}$ at $z = 1-2$).

We note that our studies in Section 4.1.1 and 4.2 thus far imply several possibilities for the submillimeter detected QG candidates obtained from the cross-matching process in Section 4.1.1, depending on the angular scales to which the observations are sensitive. They could be the correct submillimeter counterparts to the QG candidates. There are also situations where the QG candidates are not submillimeter emitters, but are physically associated with submillimeter galaxies through effects like galaxy-galaxy lensing (e.g., Fig. 11), galaxy interaction, or clustering effects at scale of a few arcsec.

5. FAINT SUBMILLIMETER GALAXIES AMONG QG CANDIDATES

In Section 4, we matched our QGs candidates to submillimeter sources and demonstrated that fractions of the matched QG candidates are physically related to the submillimeter sources. However, the $450\ \mu\text{m}$ and $850\ \mu\text{m}$ sources have a detection limit of about 3.5 mJy and 2 mJy, respectively, which correspond to SFR of roughly 60 and $180\ M_{\odot}\ \text{year}^{-1}$ at $z = 1$. Therefore, we further perform stacking analysis in order to search for fainter submillimeter emissions among the QG candidates.

5.1. Stacking Analysis

We measured the submillimeter emission from the SCUBA-2 maps at the positions of our selected QG candidates and calculated the error-weighted average of their fluxes. As our sources are point-like under JCMT’s resolution and the SCUBA-2 maps were beam-matched to produce maximum-likelihood flux for point sources, fluxes are measured by directly reading the map values in Jy beam^{-1} at the positions of the QGs. We excluded QG candidates that we matched to the bright

submillimeter sources in Section 4.1, as well as QG candidates whose measured SCUBA-2 fluxes exceed 3σ , in order to prevent our results from being biased by the small number of bright submillimeter sources. To estimate the bias and uncertainty in such a stacked flux, we then stacked at 1,000 random positions and repeated this 10,000 times. In this process, bright submillimeter sources are removed according to the same criteria as above. The mean from these random stacks is considered as the bias in stacking. It is consistent with zero, because of the zero-sum nature of the match-filtered SCUBA-2 maps. Nevertheless, this small bias is subtracted from the mean of the QGs. The dispersion among the 10,000 measurements of the random samples is considered as the uncertainty of stacking 1,000 sources. It is scaled by $1/\sqrt{N}$ to be the uncertainty of the QG stacking. We also stacked different numbers of random sources to verify this $1/\sqrt{N}$ dependence.

The stacking results are shown in Table 5 and Table 6. The first rows of the two tables show that we can reach a 6.3σ statistical detection at $850\ \mu\text{m}$ if we simply stack all QG candidates, but not a significant detection at $450\ \mu\text{m}$. The non-detection at $450\ \mu\text{m}$ may be due to the smaller coverage of the STUDIES map. Furthermore, we can divide the QG candidates into subgroups according to their properties, to see if there is a particular group of QGs that contributes to the majority of the stacked signal. First, we classified QG candidates either with $24\ \mu\text{m}$ counterparts or with 3 GHz counterparts labeled with SFG flags in the VLA catalog (Smolčić et al. 2017b) as “IR-radio-bright” QGs, and the rests as “IR-radio-faint” QGs. Our terminology is similar but slightly different from that in Man et al. (2016). Man et al. (2016) defined QG candidates with SFR derived from $24\ \mu\text{m}$ over $100\ M_{\odot}\ \text{year}^{-1}$ as “IR-bright” QGs, and the rests as “IR-faint” QGs. They used $24\ \mu\text{m}$ data and SFR constraints to classify the subgroups, while we used $24\ \mu\text{m}$ data, 3 GHz data, and radio AGN classification in our work. Then, for the $850\ \mu\text{m}$ stacking, because of the larger area of the SCUBA-2 map and therefore more available QGs, we can further divide the QG sample into various redshift and stellar mass bins.

Overall, we see that QG candidates with $24\ \mu\text{m}$ counterparts and QG candidates with 3 GHz counterparts that are not radio AGNs (i.e., IR-radio-bright QGs) exhibit the strongest stacking signal at both $450\ \mu\text{m}$ and $850\ \mu\text{m}$. These IR-radio-bright QGs account for $9.7\pm 0.2\%$ (1769/18304) of all the QG candidates. In general, we do not reach significant detections of IR-radio-faint QGs. However, even with the low SNR, the stacked $850\ \mu\text{m}$ fluxes for high-mass ($> 10^{10.5}\ M_{\odot}$) IR-radio-faint QGs are consistently higher than those for

low-mass IR-radio-faint QGs. This suggests that even the IR-radio-faint QGs have dust emission in the rest-frame far-IR, or they are clustered around dusty objects (see below). On the other hand, among IR-radio-bright QGs, it is not apparent that the high-mass ones show consistently higher $850\ \mu\text{m}$ fluxes than the low-mass ones. This suggests that we are not seeing a population of well-behaved galaxies who follow the star-formation main sequence. This is expected for QGs.

We can compare our stacked $450\ \mu\text{m}$ fluxes with the *Herschel* $500\ \mu\text{m}$ stacked fluxes in Man et al. (2016). Our mean $450\ \mu\text{m}$ flux of IR-radio-faint QGs is $0.00\pm 0.02\ \text{mJy}$, whose 1σ upper limit is over 10 times lower than their stacked $500\ \mu\text{m}$ fluxes of IR-faint QGs, which range from 0.2 to 2.5 mJy in different mass and redshift bins. The difference of defining the two QG subsamples (SFR derived from $24\ \mu\text{m}$ to be under or over $100\ M_{\odot}\ \text{year}^{-1}$ in Man et al. (2016)) may be one of the possible explanations. However, our mean $450\ \mu\text{m}$ flux of IR-radio-bright QGs, $0.65\pm 0.15\ \text{mJy}$, is still lower than most of the above mean $500\ \mu\text{m}$ fluxes of IR-faint QGs (0.2 to 2.5 mJy) except for some of those with $M_{*} < 10^{10.6}\ M_{\odot}$.

Our stacked $450\ \mu\text{m}$ fluxes are also lower compared with results in Magdis et al. (2021). They selected QG candidates with several color-color diagrams and stacked samples without $24\ \mu\text{m}$ detection, so we compare our stacked fluxes of IR-radio-faint QGs with their results. Their stacked *Herschel* $500\ \mu\text{m}$ fluxes, ranging from 0.12 to 0.59 mJy in various redshift bins, are also much higher than our stacked $450\ \mu\text{m}$ flux, $0.00\pm 0.02\ \text{mJy}$. On the other hand, their stacked SCUBA-2 $850\ \mu\text{m}$ fluxes, ranging from 0.04 to 0.1 mJy, are at a similar level as our stacked $850\ \mu\text{m}$ fluxes.

A possible explanation for the differences between the SCUBA-2 $450\ \mu\text{m}$ and *Herschel* $500\ \mu\text{m}$ stacked fluxes is that the stacked *Herschel* fluxes were biased by source clustering at the scale of the large $35''$ *Herschel* $500\ \mu\text{m}$ beam (e.g., Viero et al. 2013, also see discussion in Béthermin et al. 2017). Although Magdis et al. (2021) modeled the emission of all the stacked images to separate surrounding sources, it appears that their $500\ \mu\text{m}$ stacked fluxes are higher. Although Man et al. (2016) applied SIMSTACK to stack and deblend simultaneously, it remains possible that the effects of source blending and clustering were not completely removed.

The above comparison confirms the well known bias in submillimeter stacking analysis: when source are clustered at scales comparable to the beam size, the stacked flux would be overestimated. This bias becomes quite severe under *Herschel*’s large beams in the two longest wavebands. How about our SCUBA-2 stacked fluxes? In

Table 5. 450 μm QG Stacking Results

Groups	$\log M_*$ ^a ($\log(M_\odot)$)	z ^b	Number	$S_{450\mu\text{m}}$ (mJy)	SNR	$\log(L_{\text{IR}})$ ($\log(L_\odot)$)	$\text{SFR}_{450\mu\text{m}}$ ($M_\odot \text{ yr}^{-1}$)	$\text{SFR}_{\text{optical}}$ ^c ($M_\odot \text{ yr}^{-1}$)
All QG	$10.7^{+0.3}_{-1.1}$	0.9	1799	0.06 ± 0.05	1.3	$9.3^{+0.3}_{-0.7}$	0.2 ± 0.2	$2.5^{+0.0}_{-0.0}$
24- μm counterpart	$10.9^{+0.3}_{-0.7}$	0.8	155	0.66 ± 0.16	4.1	$10.6^{+0.1}_{-0.1}$	3.6 ± 0.9	$11.2^{+0.4}_{-0.3}$
3-GHz counterpart	$11.2^{+0.2}_{-0.4}$	0.9	103	0.60 ± 0.20	3.0	$10.5^{+0.1}_{-0.2}$	3.5 ± 1.2	$9.5^{+0.4}_{-0.4}$
3-GHz counterpart: SFG	$11.1^{+0.2}_{-0.4}$	0.9	45	0.85 ± 0.30	2.8	$10.8^{+0.1}_{-0.2}$	6.4 ± 2.3	$10.3^{+0.8}_{-0.7}$
3-GHz counterpart: AGN	$11.2^{+0.2}_{-0.3}$	0.9	58	0.39 ± 0.26	1.5	$10.2^{+0.2}_{-0.5}$	1.5 ± 1.0	$8.9^{+0.5}_{-0.6}$
IR-radio-faint QG	$10.6^{+0.3}_{-1.1}$	0.9	1620	0.00 ± 0.05	0.0	$0.0^{+9.3}_{-0.0}$	0.0 ± 0.2	$1.7^{+0.0}_{-0.0}$
IR-radio-bright QG	$11.0^{+0.3}_{-0.6}$	0.8	179	0.65 ± 0.15	4.3	$10.6^{+0.1}_{-0.1}$	3.6 ± 0.8	$10.2^{+0.4}_{-0.2}$

^aMean and 68% interval of stellar mass in logarithmic scale.

^bMedian of redshift.

^cMean of SFRs from COSMOS2015. The error shows the typical error in COSMOS2015 scaled by $1/\sqrt{N}$. Uncertainty of template fitting is not included, which may be large for QG population.

the previous section, we showed that QG candidates are clustered around 850 μm sources at scales of SCUBA-2’s beam. So if we blindly stack these QGs in the 850 μm image, the stacked flux will be overestimated. Fortunately, the majority of our 850 μm stacking signal comes from the IR-radio-bright subsample. Their 24 μm and 3 GHz counterparts are likely to be 850 μm sources themselves, and the bias caused by clustering should therefore be negligible. On the other hand, the IR-radio-faint sample does not have deep high-resolution data to confirm that the QGs are responsible for the detected 850 μm fluxes. Therefore, strictly speaking, our stacked 850 μm fluxes for IR-radio-faint QGs should be considered as upper-limits. Even if a detection is reached on certain subsample of IR-radio-faint QGs, the detected flux should be only an indication that these QG candidates are physically related to faint submillimeter emitters, rather than evidence for in situ star formation in the QG candidates.

Finally, we can examine if the strong 850 μm detection (8.6σ) of the IR-radio-bright QGs really come from galaxies in the QG color-color space in the $NUV-r-J$ diagram, or from galaxies originally in the SFG color space scattered by photometric errors across the selection boundary. In Section 3, we show that such SFG contamination caused by photometric errors account for about 7.5% of the selected QGs. With the same method, the estimated fraction for misidentified IR-radio-bright QGs caused by photometric errors is slightly higher, 8.9%. Moreover, we identified individual IR-radio-bright QGs whose probability of being scattered from the SFG color space to be > 0.05 . These sources account for 33% of our IR-radio-bright QGs (584/1769). We ex-

cluded them and re-did the stacking on the remaining IR-radio-bright QGs, and still obtained a strong detection of 0.22 ± 0.04 mJy (5.9σ) despite the very generous probability cut of > 0.05 . These results imply that misidentified QG candidates due to photometric errors account for only $< 10\%$ of our estimated dusty SFG contamination, and this minor population does not dominate our stacking results. The majority of the dusty SFG contamination is caused by their intrinsic properties rather than photometric errors.

5.2. Examining the Quiescence

To examine if our sub-samples are consistent with a quiescent population, we need to derive their SFRs and compare with their stellar masses.

We calculated the IR luminosity from the mean submillimeter fluxes and the median redshift of each group of the stacking sample. Since we only conducted measurements at 450 and 850 μm , we performed single-band SED “fitting” by assuming that there is a unique relation between SED shape and IR luminosity. To do so, we adopt the luminosity-dependent dust SED templates of J. K. Chu et al. (in preparation), which are based on the latest *WISE* and *Herschel* photometry for 201 local IR-selected galaxies (Chu et al. 2017). This set of templates covers IR luminosity of 7×10^9 to $1.7 \times 10^{12} L_\odot$. We further supplement the submillimeter galaxy SED from the zLESS program (Danielson et al. 2017), which has an IR luminosity of $5.2 \times 10^{12} L_\odot$. We redshift these SEDs to the redshifts of our targets and calculated their observed 450 μm or 850 μm fluxes. We picked the templates with redshifted fluxes closest to our stacked flux and interpolate between the template fluxes to obtain

Table 6. 850 μm QG Stacking Results

Groups	$\log M_*$ ^a ($\log(M_\odot)$)	z ^b	Number	$S_{850\mu\text{m}}$ (mJy)	SNR	$\log(L_{\text{IR}})$ ($\log(L_\odot)$)	$\text{SFR}_{850\mu\text{m}}$ ($M_\odot \text{ yr}^{-1}$)	$\text{SFR}_{\text{optical}}$ ^c ($M_\odot \text{ yr}^{-1}$)
All QG	$10.7^{+0.3}_{-1.0}$	0.9	18011	0.06 ± 0.01	6.3	$10.0^{+0.1}_{-0.1}$	1.0 ± 0.2	$3.0^{+0.0}_{-0.0}$
24- μm counterpart	$10.9^{+0.3}_{-0.6}$	0.8	1538	0.27 ± 0.03	8.2	$11.1^{+0.0}_{-0.1}$	11.7 ± 1.4	$6.2^{+0.1}_{-0.1}$
3-GHz counterpart	$11.1^{+0.2}_{-0.4}$	0.9	1028	0.14 ± 0.04	3.5	$10.8^{+0.1}_{-0.1}$	6.8 ± 1.9	$6.1^{+0.1}_{-0.1}$
3-GHz counterpart: SFG	$11.1^{+0.2}_{-0.5}$	0.9	473	0.30 ± 0.06	5.0	$11.1^{+0.1}_{-0.1}$	13.9 ± 2.7	$7.6^{+0.2}_{-0.1}$
3-GHz counterpart: AGN	$11.2^{+0.2}_{-0.4}$	0.9	555	0.01 ± 0.05	0.1	$9.2^{+1.0}_{-9.2}$	0.2 ± 1.4	$4.9^{+0.1}_{-0.1}$
IR-radio-faint QG	$10.7^{+0.3}_{-1.0}$	0.9	16242	0.04 ± 0.01	3.8	$9.8^{+0.1}_{-0.1}$	0.7 ± 0.2	$2.6^{+0.0}_{-0.0}$
$z \leq 0.5$								
$\log M_* \leq 10.5$	$9.8^{+0.4}_{-1.6}$	0.3	2399	-0.01 ± 0.03	-0.4	$0.0^{+9.3}_{-0.0}$	0.0 ± 0.2	$0.0^{+0.0}_{-0.0}$
$\log M_* > 10.5$	$10.9^{+0.1}_{-0.3}$	0.4	632	0.07 ± 0.05	1.4	$9.8^{+0.2}_{-0.6}$	0.7 ± 0.5	$0.1^{+0.0}_{-0.0}$
$0.5 < z \leq 1.0$								
$\log M_* \leq 10.5$	$10.1^{+0.3}_{-0.6}$	0.8	3739	0.01 ± 0.02	0.4	$9.2^{+0.6}_{-9.2}$	0.2 ± 0.4	$0.4^{+0.0}_{-0.0}$
$\log M_* > 10.5$	$10.9^{+0.2}_{-0.3}$	0.8	3375	0.05 ± 0.02	2.2	$9.9^{+0.2}_{-0.3}$	0.8 ± 0.4	$0.3^{+0.0}_{-0.0}$
$1.0 < z \leq 1.5$								
$\log M_* \leq 10.5$	$10.2^{+0.2}_{-0.3}$	1.2	1461	-0.02 ± 0.03	-0.5	$0.0^{+9.8}_{-0.0}$	0.0 ± 0.6	$2.1^{+0.0}_{-0.0}$
$\log M_* > 10.5$	$10.9^{+0.2}_{-0.3}$	1.2	2351	0.09 ± 0.03	3.4	$10.6^{+0.1}_{-0.2}$	3.6 ± 1.0	$1.1^{+0.0}_{-0.0}$
$1.5 < z \leq 2.0$								
$\log M_* \leq 10.5$	$10.3^{+0.2}_{-0.2}$	1.7	469	0.07 ± 0.06	1.3	$10.3^{+0.3}_{-0.7}$	2.1 ± 1.7	$12.6^{+0.5}_{-0.3}$
$\log M_* > 10.5$	$10.9^{+0.2}_{-0.3}$	1.7	1234	0.08 ± 0.04	2.3	$10.6^{+0.2}_{-0.2}$	3.7 ± 1.6	$8.9^{+0.1}_{-0.1}$
$2.0 < z \leq 2.5$								
$\log M_* \leq 10.5$	$10.3^{+0.2}_{-0.2}$	2.3	107	0.11 ± 0.12	0.9	$10.5^{+0.3}_{-10.5}$	2.9 ± 3.2	$25.5^{+2.5}_{-1.5}$
$\log M_* > 10.5$	$10.9^{+0.2}_{-0.3}$	2.3	260	0.25 ± 0.08	3.2	$11.1^{+0.1}_{-0.2}$	12.8 ± 4.0	$29.1^{+1.3}_{-0.8}$
$z > 2.5$								
$\log M_* \leq 10.5$	$10.3^{+0.1}_{-0.1}$	2.7	47	-0.05 ± 0.19	-0.3	$0.0^{+11.0}_{-0.0}$	0.0 ± 10.0	$25.5^{+4.4}_{-2.1}$
$\log M_* > 10.5$	$10.9^{+0.2}_{-0.3}$	2.7	168	0.11 ± 0.10	1.1	$10.8^{+0.3}_{-0.9}$	6.0 ± 5.3	$37.3^{+2.5}_{-1.4}$
IR-radio-bright QG	$11.0^{+0.2}_{-0.6}$	0.9	1769	0.26 ± 0.03	8.6	$11.1^{+0.0}_{-0.1}$	11.7 ± 1.4	$6.4^{+0.1}_{-0.1}$
$z \leq 0.5$								
$\log M_* \leq 10.5$	$10.1^{+0.3}_{-1.5}$	0.3	90	0.28 ± 0.13	2.0	$10.8^{+0.2}_{-0.3}$	6.8 ± 3.3	$0.2^{+0.0}_{-0.0}$
$\log M_* > 10.5$	$11.1^{+0.2}_{-0.4}$	0.4	214	0.14 ± 0.09	1.6	$10.3^{+0.2}_{-0.4}$	2.0 ± 1.2	$0.4^{+0.0}_{-0.0}$
$0.5 < z \leq 1.0$								
$\log M_* \leq 10.5$	$10.2^{+0.2}_{-0.3}$	0.8	220	0.24 ± 0.09	2.8	$11.0^{+0.1}_{-0.2}$	10.5 ± 3.8	$5.1^{+0.1}_{-0.1}$
$\log M_* > 10.5$	$11.1^{+0.2}_{-0.4}$	0.8	730	0.13 ± 0.05	2.7	$10.5^{+0.1}_{-0.2}$	3.0 ± 1.1	$1.7^{+0.0}_{-0.0}$
$1.0 < z \leq 1.5$								
$\log M_* \leq 10.5$	$10.3^{+0.2}_{-0.3}$	1.2	44	0.39 ± 0.19	2.0	$11.3^{+0.2}_{-0.3}$	21.1 ± 10.5	$8.7^{+1.0}_{-0.5}$
$\log M_* > 10.5$	$11.1^{+0.2}_{-0.4}$	1.2	260	0.40 ± 0.08	5.1	$11.4^{+0.1}_{-0.1}$	22.6 ± 4.5	$3.6^{+0.2}_{-0.1}$
$1.5 < z \leq 2.0$								
$\log M_* \leq 10.5$	$10.3^{+0.1}_{-0.1}$	1.6	27	0.62 ± 0.25	2.5	$11.9^{+0.1}_{-0.2}$	80.9 ± 32.3	$28.6^{+4.9}_{-2.2}$
$\log M_* > 10.5$	$11.0^{+0.2}_{-0.4}$	1.7	108	0.81 ± 0.12	6.6	$12.0^{+0.1}_{-0.1}$	102.3 ± 15.6	$21.1^{+0.8}_{-0.7}$
$2.0 < z \leq 2.5$								
$\log M_* \leq 10.5$	$10.3^{+0.1}_{-0.2}$	2.2	6	1.25 ± 0.52	2.4	$12.1^{+0.2}_{-0.2}$	128.8 ± 54.0	$65.8^{+14.3}_{-15.2}$
$\log M_* > 10.5$	$11.1^{+0.2}_{-0.4}$	2.2	39	0.48 ± 0.20	2.4	$11.6^{+0.2}_{-0.2}$	38.6 ± 16.3	$61.1^{+5.7}_{-3.5}$
$z > 2.5$								
$\log M_* \leq 10.5$	$10.5^{+0.0}_{-0.0}$	2.7	2	0.42 ± 0.90	0.5	$11.4^{+0.5}_{-11.4}$	28.1 ± 60.4	$27.8^{+17.4}_{-9.9}$
$\log M_* > 10.5$	$11.0^{+0.2}_{-0.4}$	2.8	27	0.44 ± 0.25	1.8	$11.5^{+0.2}_{-0.4}$	30.8 ± 17.1	$62.5^{+11.6}_{-6.6}$

^{abc}The parameters follow those in Table 5.

the IR luminosity of our targets. We scaled the IR luminosity by $1/\text{SNR}$ to estimate 1σ error of the IR luminosity. For groups with negative mean flux, we calculated the corresponding IR luminosity of flux error to estimate 1σ upper limit of the IR luminosity. The results are presented in the seventh columns of Tables 5 and 6.

To verify the results based on the local SEDs of Chu et al., we also repeated the calculations using the SED library of Schreiber et al. (2018a). Overall, we find no systematic differences if we assume main sequence galaxies ($R_{\text{SB}} = 1$) for the Schreiber et al. library. The mean difference in the calculated L_{IR} is less than 0.1 dex for the non-zero entries in Tables 5 and 6, while the rms dispersion is within 0.25 dex. This small difference can be further reduced if we assume a sub-main-sequence R_{SB} for the IR-radio-faint subsamples in Table 6 and a starburst R_{SB} for the IR-radio-bright subsamples. This tuning of the R_{SB} parameter is consistent with our interpretation of these two subgroups (see below). In our subsequent analyses, we adopt the calculations based on the SEDs of Chu et al.

After calculating the IR luminosity, we followed the L_{IR} -SFR calibration applied in Man et al. (2016). We estimate the SFR by applying the relation applicable for SFGs (Kennicutt 1998):

$$\text{SFR}(M_{\odot} \text{ yr}^{-1}) = 1.7 \times 10^{-10} L_{\text{IR}}(L_{\odot}).$$

We then adjusted the obtained SFR to the Chabrier (2003) IMF by applying the calibration used in Man et al. (2016):

$$\text{SFR}_{\text{Chabrier}} = \text{SFR}_{\text{Salpeter}}/1.7$$

The results are presented in the eighth columns of Table 5 and Table 6 as $\text{SFR}_{450\mu\text{m}}$ and $\text{SFR}_{850\mu\text{m}}$, respectively. A few observations can be made here. First, the 850- μm derived SFR is in general higher than the 450- μm derived SFR. This is partly caused by the much deeper in luminosity sensitivity of the SCUBA-2 450 μm imaging and the $< 3\sigma$ thresholds we imposed in the stacking procedure. If we remove this threshold in the 450 μm imaging, the difference reduces to within a factor of 2, which is not very significant if we consider the overall low S/N of the 450 μm stacked fluxes and the small number of available sources for the 450 μm stacking.

We compare our results with SFRs derived from optical SED fitting in COSMOS2015 (last column in Table 5 and 6). Their mean SFRs of IR-radio-faint QGs are higher than ours at high z but their mean SFRs of IR-radio-bright QGs are lower. This can be explained with the age-extinction degeneracy in the SED fitting when there is an absence of far-IR photometry.

We compare the submillimeter-derived SFRs with the stellar masses of the galaxies in Fig. 7. We show the star-formation “main sequence” of Speagle et al. (2014) with black solid lines and the ± 0.9 dex ranges with shaded areas.

We show the results from Man et al. (2016) for comparison (Fig. 7). Our results are in broad agreement with theirs but tend to have slightly lower SFR for low- z samples. In the $0.5 < z \leq 1.0$ and $1.0 < z \leq 1.5$ redshift bins, their massive IR-bright QGs are located on or ~ 1 to 2σ above the main sequence, while our IR-radio-bright QGs are located ~ 2 to 3σ below the main sequence. Their IR-faint QGs are located $\sim 3\sigma$ below the main sequence, while our IR-radio-faint QGs are located $> 3\sigma$ below the main sequence. Other than these, our derived SFRs are fairly consistent. We note that the SFR of Man et al. (2016) was derived from SED fitting using stacked fluxes across the entire far-IR range. This explains why their 500 μm stacked fluxes are much higher than ours, but their SFRs are not.

We also show the results from Magdis et al. (2021) in Fig. 7. Their SFRs are about the same as or slightly lower than our SFRs, different from the comparison with Man et al. (2016). We note that their IR luminosities were derived from SED fitting using stacked fluxes from mid-IR to radio data. They then also obtained SFRs by applying the relation in Kennicutt (1998), but they used a Salpeter IMF and added SFR derived from the optical photometry. We converted their IR luminosity to SFR by the same process in Man et al. (2016) and this work for a fair comparison. We also show their SFRs obtained by the original conversion in their work for reference, which are in general closer to the SFRs from Man et al. (2016).

The conclusion we can draw from Fig. 7 is that the IR-radio-faint QGs are in general below the star-formation main sequence, while the majority of the IR-radio-bright QGs are consistent with the main sequence, probably except for the high-mass end in the two low-redshift bins and in the highest redshift bin.

To sum up, our stacking results show that only the IR-radio-bright QGs have SFR similar to main-sequence galaxies. These are likely to be faint dusty SFGs that contaminate the QG color selection. However, the population of the IR-radio-bright QGs is small, which accounts for $9.7 \pm 0.7\%$ (179/1846) and $9.7 \pm 0.2\%$ (1769/18304) of all the QG candidates, respectively, in the 450 and 850 μm images. The fractions range from 7% to 12% in different redshift bins and do not have a strong redshift dependence. We conclude that the contamination of dusty SFGs is of $\sim 10\%$ among the color-selected QG candidates, and that the contamination can

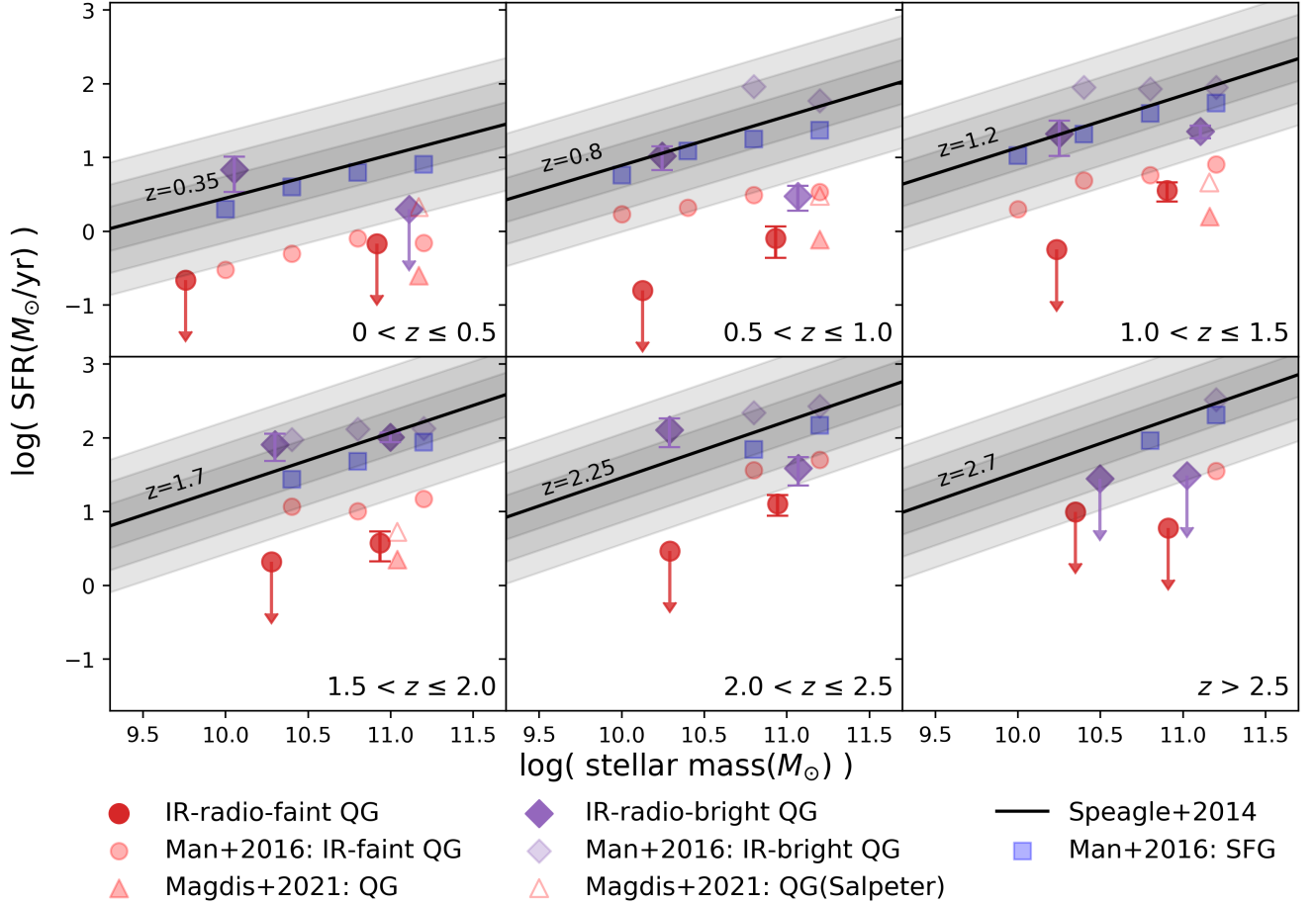


Figure 7. SFR derived from $850\ \mu\text{m}$ fluxes versus stellar mass. The purple diamonds represent IR-radio-bright QGs, while the red circles represent IR-radio-faint QGs. The smaller semi-transparent symbols are results from other works. The purple diamonds, red circles, and blue squares represent the IR-bright QGs, IR-faint QGs, and SFGs in [Man et al. \(2016\)](#), respectively. The red triangles represent QGs in [Magdis et al. \(2021\)](#). IR-radio-bright QGs in our work are defined as QG candidates either with $24\ \mu\text{m}$ counterparts or with 3 GHz counterparts labeled with SFG flags in the VLA catalog ([Smolčić et al. 2017b](#)), while IR-bright QGs in [Man et al. \(2016\)](#) are defined as QG candidates with SFR derived from $24\ \mu\text{m}$ over $100\ M_{\odot}\ \text{year}^{-1}$. QGs in [Magdis et al. \(2021\)](#) are defined as QG candidates without $24\ \mu\text{m}$ detection. The filled triangles are derived by the same L_{IR} -SFR conversion with the other two works, while the open triangles are derived by the conversion described in their work. The black solid line shows the SFR of the redshift-dependent main sequence with a $1\text{--}3 \times 0.3$ dex scatters in [Speagle et al. \(2014\)](#).

be removed using multi-wavelength data such as the $24\ \mu\text{m}$ and 3 GHz data for the COSMOS field.

For comparison, [Man et al. \(2016\)](#) suggested that the maximum contamination is 15% and could be removed by using $24\ \mu\text{m}$ observations. In this study, we used submillimeter data with better sensitivities and resolutions, and our estimate of contamination is somewhat tighter (10%) than that in [Man et al. \(2016\)](#).

Like what we did in Section 4.1.1, if we assume the same fraction of QGs among AS2COSMOS sources, we can estimate the number of faint submillimeter sources that are QGs. For the number of faint submillimeter sources, we again applied the $850\ \mu\text{m}$ number count in [Simpson et al. \(2019\)](#) and extrapolated it to a flux level

of $S_{850\mu\text{m}} = 0.5\ \text{mJy}$. This leads to 707 ± 462 QGs among faint submillimeter sources, and a dusty galaxy contamination rate among QGs of $3.9 \pm 2.5\%$. We can further extrapolate the counts to $0.26\ \text{mJy}$, the stacked $850\ \mu\text{m}$ flux of IR-radio-bright QGs. This will further increase the estimated contamination rate. However, such an extrapolation is probably too aggressive given the uncertainty in the faint-end counts. Nevertheless, considering the unknown uncertainty of extrapolating the number count to a flux level lower than the detection limit, we concluded that the above estimation is not inconsistent with the $\sim 10\%$ contamination derived from the stacking of IR-radio-bright QGs.

Finally, using either 24 μm or 3 GHz data to pinpoint star-forming contaminants among color-selected QG candidates may not work well at high redshifts ($z > 3$ or 4). This is because mid-IR and radio suffer from the strong K -correction and are not sensitive to high-redshift SFGs. Our 3.4σ detection in the 850 μm stacking of the IR-radio-faint QGs at $z > 2$ seems to agree with this, i.e., there may exist dusty galaxy contamination that are faint in the mid-IR and radio. In other words, the effectiveness of QG color selection at high redshift remains untested in this framework. Since the formation of QGs at higher redshifts require both rapid growth of the stellar population and rapid quenching, identifications of high-redshift QGs are of great interest (Merlin et al. 2018; Straatman et al. 2014; Carnall et al. 2020; Valentino et al. 2020). Removing dusty contaminants among high-redshift QGs is beyond the sensitivities of *Spitzer*, *Herschel*, and the current VLA, and will require deep ALMA data.

6. AGN PROPERTIES

In this section, we discuss the properties of the AGNs among our QG candidates. Fig. 8 shows the distribution of three different classes of AGN samples in the $NUV-r-J$ diagram, including radio AGNs, mid-IR AGNs, and X-ray AGNs (Section 2.4) in two mass bins. The stellar mass of the samples were limited to above $10^{10.5} M_{\odot}$. This is because the samples are likely to be incomplete below $10^{10.5} M_{\odot}$ at $z \sim 2$ (see Fig. 2 (b)). This mass limit is also consistent with the 90% completeness limit found by Laigle et al. (2016) for QGs at high redshifts. We therefore applied this stellar mass cut for fair comparisons of the QG fractions. In Fig. 8, we can see that the distribution of the radio AGNs is different from those of the other two. A similar distinction also exists between radio selected sources and 24 μm selected sources in Fig. 3. Fig. 8 provides evidence that the difference in Fig. 3 is driven by radio AGNs.

We calculated the QG fractions in different classes of the AGN samples in different redshift and mass bins (Fig. 9). The QG fraction of the radio AGNs is (~ 0.1 to 1.9σ) higher than that of the non-AGN samples at $z < 1.5$ in both two mass bins, while the QG fractions of the other two AGN classes are significantly lower. The trend does not persist beyond $z \sim 1.5$, and this may be due partially to the detection limit of the radio AGNs, or a real redshift evolution. The high QG fraction among radio AGNs implies a correlation between radio jets and our QG candidates.

We also calculated the AGN fractions in our COSMOS2015 sample (Fig. 10). The radio AGN fraction among QG candidates is (~ 0.2 to 1.7σ) higher than that

among the COSMOS2015 QG and SFG sample, also at $z < 1.5$ and in both two mass bins. The situations are the opposite for both the mid-IR and X-ray AGNs, where the AGN fractions among the QG+SFG sample are higher. The higher radio AGN fraction among QGs also suggests a correlation between radio jets and our QG candidates.

The above correlation between radio AGNs and QGs may provide some clues about the quenching mechanism. Our data suggest that the formation of radio jets and quenching of star formation are connected, but the exact causality is unclear. One possible scenario is that radio-mode AGN feedback, particularly radio jets with high kinetic energy, could have impacts on the host galaxy and its environment (Croton et al. 2006; Bower et al. 2006; Fabian 2012; Somerville et al. 2008; Wagner & Bicknell 2011). Either the interstellar medium in the host galaxy may be disrupted by the jets (e.g., Fabian 2012; Somerville et al. 2008), or the gas in the halo can be heated up and be prevented from cooling and falling onto the host galaxy (e.g., Croton et al. 2006; Bower et al. 2006; Somerville et al. 2008). Although the radio AGNs fraction is only ~ 10 to 20% among QG candidates (Fig. 10), this can be explained by the AGN duty cycle in the massive galaxies.

On the other hand, it is also possible that radio AGNs are not directly linked to the quenching process. Instead, it may be just easier to trigger radio AGNs in galaxies that are already quenched. In the local universe, it is well known that there is a dominant tendency for radio galaxies to reside in early-type hosts (e.g., Govoni et al. 2000; Hamilton et al. 2002), which is consistent with what we found on QGs and radio AGNs. The lack of cool gas in early-type (quenched) galaxies can lead to radiatively inefficient accretion that is associated with the radio mode AGN feedback (Croton et al. 2006; Bower et al. 2006; Somerville et al. 2008).

Observationally, the stacking result in Man et al. (2016) also showed a similar trend. The authors compared the radio stacked fluxes and the *Herschel* stacked fluxes of their sample. Their SFRs derived from the two are consistent for SFGs, but there exists a radio excess for massive IR-faint QGs with $M_* \geq 10^{11} M_{\odot}$ at $z < 1.5$. They further measured the FIR-to-radio luminosity ratio and concluded that most of their massive QGs host low-luminosity radio AGNs. Also, Smolčić et al. (2009) found that the radio AGN fraction among red galaxies increases from $z \sim 0.5$ to 1, showing that radio AGNs play an important role at $z \sim 1$. It is also known that SFR is correlated with AGN accretion rate (Zhuang & Ho 2020), and that low-accretion rate AGNs are radio-loud (Ho 2002, 2008). This implies that QGs tends to

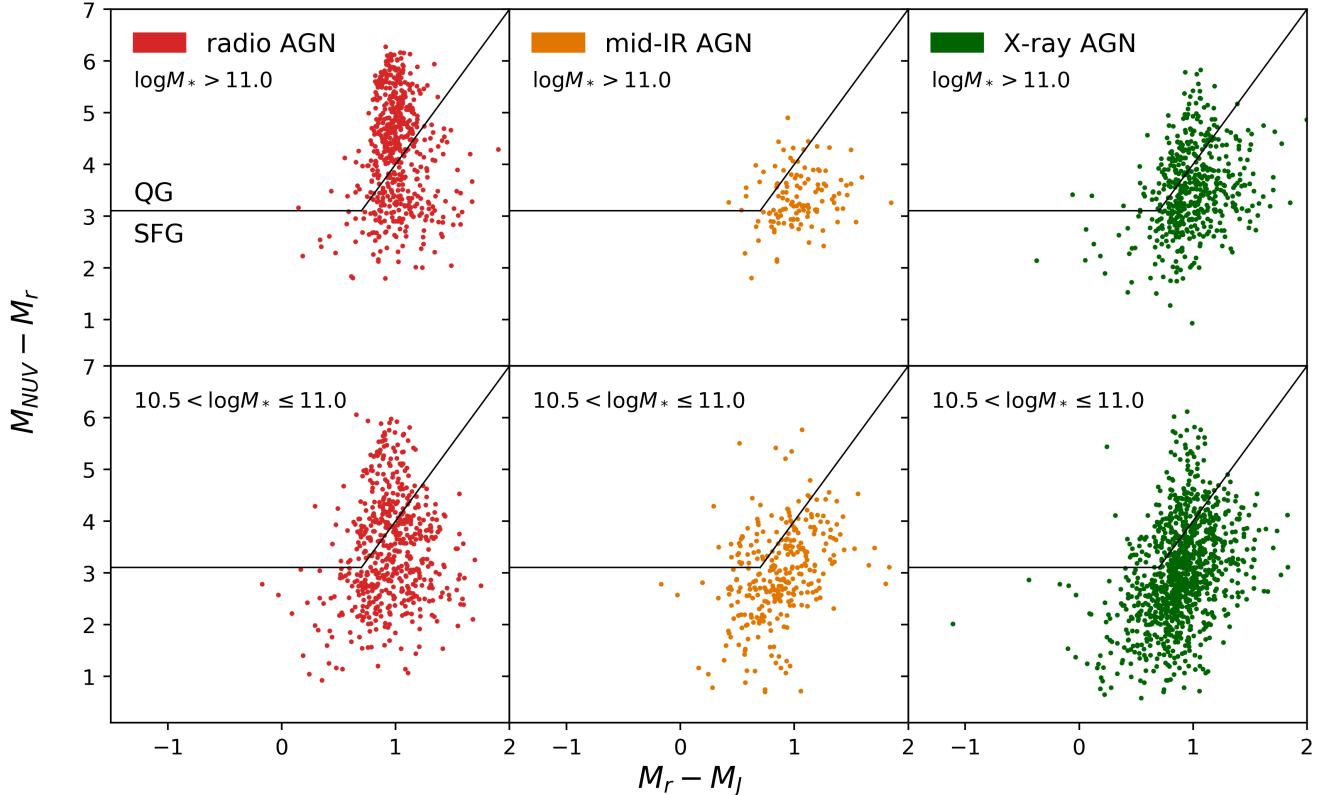


Figure 8. The distribution of radio AGNs (left panels), mid-IR AGNs (middle panels), and X-ray AGNs (right panels) on the $NUV-r-J$ diagram with $M_* > 10^{11} M_\odot$ (top panels) and $10^{10.5} M_\odot < M_* \leq 10^{11.0} M_\odot$ (lower panels).

be radio AGNs. All these results suggest that there is a correlation between QGs and synchrotron radiation from radio AGNs.

We could also see a weak correlation between X-ray AGNs and QG candidates at $z > 2.5$. In Fig. 9, the QG fractions among X-ray AGNs are ~ 0.6 to 1.5σ larger than those among non AGNs in $z > 2.5$ redshift bins, with respect to their own error bars. In Fig. 10, the AGN fraction among QGs is $\sim 0.9\sigma$ larger than that among the full sample in the $z > 2.5$ and $M_* > 10^{11} M_\odot$ bin. This may be caused by either selection bias or a real evolution trend. The evolution trend could be explained by the role of quasar-mode AGN feedback (Fabian 2012; Somerville et al. 2008), gas inflow in X-ray AGNs that removes gas and quenches star formation. One possibility is that the mode of AGN quenching may change from quasar-mode to radio-mode from high z to low z . Another possibility could be that X-ray AGNs are related to the initial quenching, while radio AGNs are responsible for the maintenance of the quiescence. This could also explain the increasing radio AGN fraction among QG candidates in Fig. 10 at lower redshift. Nevertheless, the rises in the X-ray AGNs in Fig. 9 and 10 only occur in the highest redshift bins where the sample sizes are the smallest and the selection completeness is less well

understood. This has to be further tested with more data and careful examination of various selection biases in the high-redshift ends.

To sum up, our data show a strong correlation between radio AGNs and QGs but do not point to the right scenario. Our data also do not show whether radio AGNs are related to the initial quenching, or just related to the maintenance of the quiescence.

7. SUMMARY

In this study, we examined the submillimeter properties of $NUV-r-J$ selected QG candidates at $z \lesssim 3$. We cross-matched the QG candidates with bright submillimeter sources detected by JCMT SCUBA-2 and ALMA. For the former, we used *Spitzer* 24 μm and VLA 3 GHz data to refine their positions to overcome the low angular resolution of JCMT. This way, we found that $0.16 \pm 0.03\%$ to $0.43 \pm 0.15\%$ among our QG candidates are likely to be bright 850 and 450 μm submillimeter galaxies, respectively. The contamination increases to $1.72 \pm 0.50\%$ to $3.51 \pm 2.48\%$ at $z > 2$. We further performed stacking analysis of QG candidates in the JCMT 450 and 850 μm images. We can obtain strong stacking detections on a subsample of QGs with *Spitzer* 24 μm and VLA 3 GHz counterparts that are not radio AGNs.

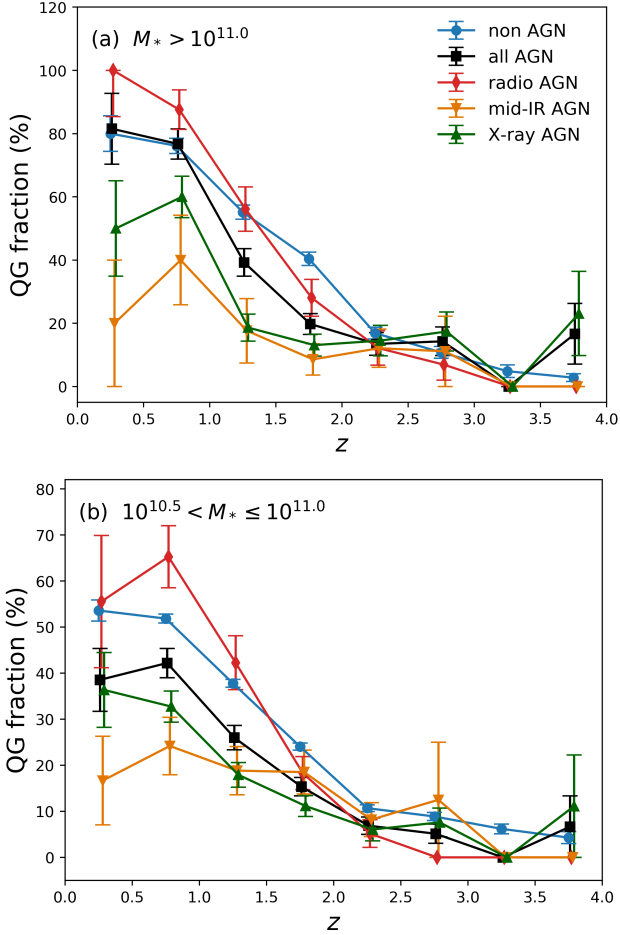


Figure 9. The QG fraction among different classes of AGN samples in redshift bins with $M_* > 10^{11} M_\odot$ (a) and $10^{10.5} M_\odot < M_* \leq 10^{11.0} M_\odot$ (b). The data points are slightly offset along x-axis for clarity. The errors are Poissonian.

This special class of “IR-radio-bright” QGs account for about 10% of the entire QG sample and they are likely to be faint submillimeter sources with SFRs of a few tens to about a hundred $M_\odot \text{ yr}^{-1}$. These results are broadly consistent with the contaminate rates derived from a small sample of ALMA detected QGs and the $850 \mu\text{m}$ number counts. We conclude that the dusty star-forming galaxy contamination rate among $NUV-r-J$ selected QG candidates is up to $\sim 10\%$, but such contamination can be removed by $24 \mu\text{m}$, submillimeter, or 3 GHz observations at current sensitivity levels.

When we cross-matched the QG candidates with JCMT SCBUA-2 $850 \mu\text{m}$ SMGs without relying on high-resolution data, we adopted a large matching radius of $7''$ because of the large SCUBA-2 beam size. This leads to a large fraction of chance projections among the matched QGs. We estimated the number of chance projections with simulations by assuming random spatial

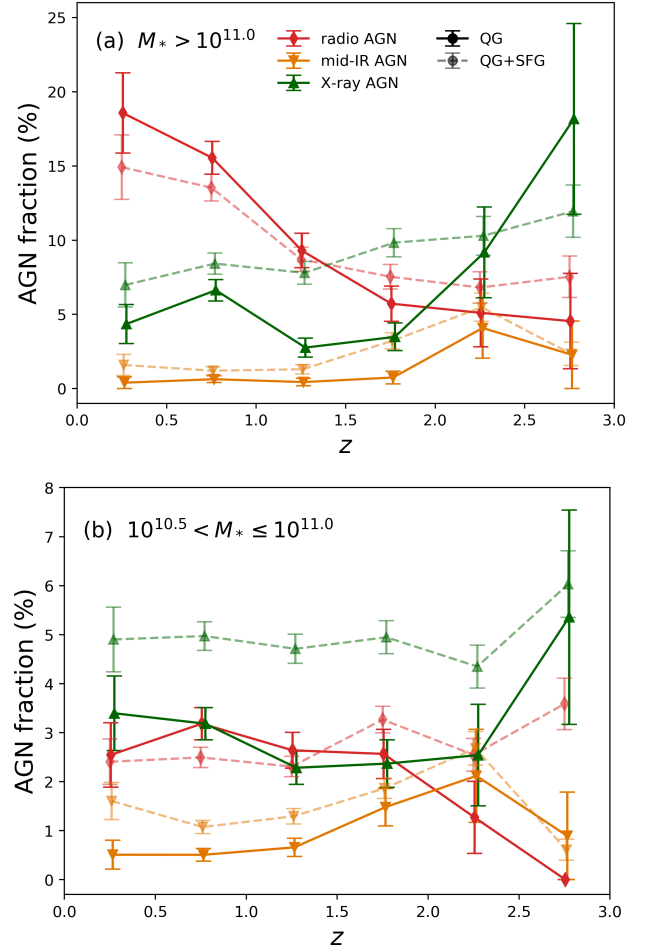


Figure 10. Different classes of AGN fraction among COSMOS2015 optical sample in redshift bins with $M_* > 10^{11} M_\odot$ (a) and $10^{10.5} M_\odot < M_* \leq 10^{11.0} M_\odot$ (b). The solid lines represent AGN fraction among QG candidates, while the dotted line represent AGN fraction among all the galaxies (QGs and SFGs). The data points are slightly offset along x-axis for clarity. The errors are Poissonian.

distributions for SCUBA-2 sources. After statistically subtracting the chance projections, we found that on average, 0.096 (35.4/370) QG is physically related to an $850 \mu\text{m}$ selected SMG, while ALMA observations indicate that only 0.026 (9.7/370) QG really coincides with an SMG within $1''$. This implies a clustering between these two populations at a scale of $1''$ to $7''$, and should be a future topic of investigation.

Finally, we examined the QG fractions among our AGN samples and found a correlation between our QG candidates and radio AGNs. When we limited our studies to galaxies with stellar masses larger than $10^{10.5} M_\odot$, we found that the QG fraction of radio AGNs are larger than those of the non-AGN samples, IR AGNs, and X-ray AGNs at $z < 1.5$. This suggests a connection be-

tween the radio jets and the quenching or the maintenance of the quiescence of the QGs, or the so-called radio-mode AGN feedback. However, our data do not rule out the possibility that radio AGNs are just more easily triggered in quenched galaxies, rather than being responsible for the initial quenching.

The authors thank Bau-Ching Hsieh, Ian Smail, Iary Davidzon, and Olivier Ilbert for the discussion and comments, the anonymous referee for the comments that greatly improve the manuscript, and JCMT staff for the observational support. Y.H.H., W.H.W., Y.Y.C., C.F.L., and Z.K.G. acknowledge grant support from the Ministry of Science and Technology of Taiwan (MoST, 105-2112-M-001-029-MY3, 108-2112-M-001-014-, and 109-2112-M-001-011-). C.C.C. acknowledges MoST grant 109-2112-M-001-016-MY3. M.J.M. acknowledges the support of the National Science Centre, Poland through the SONATA BIS grant 2018/30/E/ST9/00208. M.P.K. acknowledges support from the First TEAM grant of the Foundation for Polish Science No. POIR.04.04.00-00-5D21/18-00. L.C.H. was supported by the National Science Foundation of China (11721303, 11991052) and the National Key R&D Program of China (2016YFA0400702). Y.G. acknowledges National Science Foundation of China (NSFC) grants #11861131007, 12033004, and 11420101002, and Chinese Academy of Sciences Key Research Program of

Frontier Sciences (Grant No. QYZDJ-SSW-SLH008). The submillimeter data used in this work include observations from the JCMT Large and Legacy Programs: S2COSMOS (M16AL002), STUDIES (M16AL006), and S2CLS (MJLSC01), the JCMT PI program of Casey et al. (M11BH11A, M12AH11A, and M12BH21A), the ALMA program AS2COSMOS (ADS/JAO.ALMA #2016.1.00463.S), and various ALMA archival data. The James Clerk Maxwell Telescope is operated by the East Asian Observatory on behalf of the National Astronomical Observatory of Japan; the Academia Sinica Institute of Astronomy and Astrophysics; the Korea Astronomy and Space Science Institute; and the Operation, Maintenance and Upgrading Fund for Astronomical Telescopes and Facility Instruments, budgeted from the Ministry of Finance (MOF) of China and administrated by the Chinese Academy of Sciences (CAS), as well as the National Key R&D Program of China (No. 2017YFA0402700). Additional funding support is provided by the Science and Technology Facilities Council of the United Kingdom and participating universities in the United Kingdom and Canada. ALMA is a partnership of ESO (representing its member states), NSF (USA), and NINS (Japan), together with NRC (Canada), NSC and ASIAA (Taiwan), and KASI (Republic of Korea), in cooperation with the Republic of Chile. The Joint ALMA Observatory is operated by ESO, AUI/NRAO, and NAOJ.

APPENDIX

A. LENSED SYSTEM

One of the 850 μm detected QG candidates (ID = 659416 in the COSMOS2015 catalog; star symbol in Fig. 4) is likely to be a lensed system because of its unusual submillimeter/radio flux ratio. The K_S -band image and the ALMA image of the lensed system are shown in Fig. 11. The QG candidate is at $z = 0.36$ and is surrounded by two ALMA Band-7 sources, AS2COS0005.1 and AS2COS0005.2. The two ALMA sources have 343 GHz fluxes of 8.84 mJy and 2.20 mJy, respectively. The 3 GHz fluxes are 27.0 μJy and 7.9 μJy . These values lead to very similar 343-to-3 GHz flux ratios of 0.33, and 0.28. Under the framework of “millimetric redshift” (Carilli & Yun 1999), the similar flux ratios imply similar redshifts. The estimated redshifts are 2.7 and 2.6, if we assume a radio spectral slope of 0.8 to infer the 1.4 GHz fluxes and if we adopt the millimetric redshift formula of (Barger et al. 2000):

$$z + 1 = 0.98 \times (S_{850\mu\text{m}}/S_{1.4\text{GHz}})^{0.26}.$$

The estimated redshifts are much higher than the QG photometric redshift. Therefore, the two ALMA sources are likely to be background sources, rather than dust emission from the QG candidate. Indeed, the elongated morphology of AS2COS0005.1 (Fig. 11) and the relative positions of the two ALMA sources strongly suggest that they are multiple images of the same background dusty galaxy lensed by the foreground QG.

This target was also identified as a lensed system in Bertoldi et al. (2007) by using the same submillimeter/radio flux ratio approach. The authors measured the Max-Planck Millimeter Bolometer Array (MAMBO-2) 250 GHz flux of the target (labeled as MM J100024+021748 or Cosbo-7) and obtained $z \sim 2.8$, consistent with our estimation. Jin et al. (2018) also reported this lensed system (labeled as ID20003080) and derived a photometric redshift of 4.0 ± 0.6 from 24 μm to radio SED fitting. In our study, we further confirmed their results by including high-resolution ALMA image, which resolved the background target into two sources with elongated morphology.

We note that there are in total three QG candidates with photometric redshift lower than 1 among those matched to SCUBA-2 sources through ALMA catalogs, and we examined their millimetric redshifts. Besides the target discussed above, the other two low z targets also show higher submillimeter/radio flux ratio. However, we do not further discuss the two targets since the estimated millimetric redshifts are not significantly high.

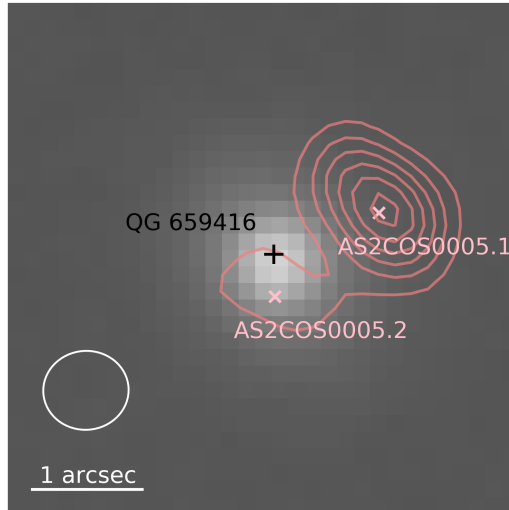


Figure 11. CFHT K_S band image and ALMA 343 GHz emission contours ($5, 10, \dots \times \sigma$) of the lensed system. The image has a size of $\sim 4.5''$ on a side. The white circle shows the ALMA beam. The black plus symbol shows the position of the QG candidate. The pink cross symbols show the positions of the ALMA sources, which are likely to be background galaxies lensed by the QG candidate or even multiple lensed images of a single background galaxy.

REFERENCES

- An, F. X., Stach, S. M., Smail, I., et al. 2018, *ApJ*, **862**, 101
- Arnouts, S., Le Floch, E., Chevallard, J., et al. 2013, *A&A*, **558**, A67
- Barger, A. J., Cowie, L. L., & Richards, E. A. 2000, *AJ*, **119**, 2092
- Belli, S., Newman, A. B., & Ellis, R. S. 2017a, *ApJ*, **834**, 18
- Belli, S., Genzel, R., Förster Schreiber, N. M., et al. 2017b, *ApJL*, **841**, L6
- Bertin, E., & Arnouts, S. 1996, *A&AS*, **117**, 393
- Bertoldi, F., Carilli, C., Aravena, M., et al. 2007, *ApJS*, **172**, 132
- Béthermin, M., Wu, H.-Y., Lagache, G., et al. 2017, *A&A*, **607**, A89
- Bower, R. G., Benson, A. J., Malbon, R., et al. 2006, *MNRAS*, **370**, 645
- Calzetti, D., Armus, L., Bohlin, R. C., et al. 2000, *ApJ*, **533**, 682
- Carilli, C. L., & Yun, M. S. 1999, *ApJL*, **513**, L13
- Carnall, A. C., McLure, R. J., Dunlop, J. S., et al. 2019, *MNRAS*, **490**, 417
- Carnall, A. C., Walker, S., McLure, R. J., et al. 2020, *MNRAS*, **496**, 695
- Casey, C. M., Chen, C.-C., Cowie, L. L., et al. 2013, *MNRAS*, **436**, 1919
- Chabrier, G. 2003, *PASP*, **115**, 763
- Chang, Y.-Y., Le Floch, E., Juneau, S., et al. 2017, *ApJS*, **233**, 19
- Chen, C.-C., Smail, I., Swinbank, A. M., et al. 2015, *ApJ*, **799**, 194
- Chu, J., Sanders, D. B., Larson, K. L., et al. 2017, in American Astronomical Society Meeting Abstracts, Vol. 230, American Astronomical Society Meeting Abstracts #230, 401.05
- Ciambur, B. C., Kauffmann, G., & Wuyts, S. 2013, *MNRAS*, **432**, 2488
- Civano, F., Marchesi, S., Comastri, A., et al. 2016, *ApJ*, **819**, 62
- Cowie, L. L., Barger, A. J., Hsu, L. Y., et al. 2017, *ApJ*, **837**, 139
- Croton, D. J., Springel, V., White, S. D. M., et al. 2006, *MNRAS*, **365**, 11

- Daddi, E., Dickinson, M., Morrison, G., et al. 2007, *ApJ*, 670, 156
- Danielson, A. L. R., Swinbank, A. M., Smail, I., et al. 2017, *ApJ*, 840, 78
- Dekel, A., Sari, R., & Ceverino, D. 2009, *ApJ*, 703, 785
- Delvecchio, I., Smolčić, V., Zamorani, G., et al. 2017, *A&A*, 602, A3
- Donley, J. L., Koekemoer, A. M., Brusa, M., et al. 2012, *ApJ*, 748, 142
- Elbaz, D., Daddi, E., Le Borgne, D., et al. 2007, *A&A*, 468, 33
- Fabian, A. C. 2012, *ARA&A*, 50, 455
- Forrest, B., Annunziatella, M., Wilson, G., et al. 2020a, *ApJL*, 890, L1
- Forrest, B., Marsan, Z. C., Annunziatella, M., et al. 2020b, *ApJ*, 903, 47
- Fumagalli, M., Labbé, I., Patel, S. G., et al. 2014, *ApJ*, 796, 35
- Glazebrook, K., Schreiber, C., Labbé, I., et al. 2017, *Nature*, 544, 71
- Gobat, R., Daddi, E., Magdis, G., et al. 2018, *Nature Astronomy*, 2, 239
- Govoni, F., Falomo, R., Fasano, G., & Scarpa, R. 2000, *A&A*, 353, 507
- Hamilton, T. S., Casertano, S., & Turnshek, D. A. 2002, *ApJ*, 576, 61
- Ho, L. C. 2002, *ApJ*, 564, 120
- . 2008, *ARA&A*, 46, 475
- Holland, W. S., Robson, E. I., Gear, W. K., et al. 1999, *MNRAS*, 303, 659
- Holland, W. S., Bintley, D., Chapin, E. L., et al. 2013, *MNRAS*, 430, 2513
- Ilbert, O., McCracken, H. J., Le Fèvre, O., et al. 2013, *A&A*, 556, A55
- Ishibashi, W., & Fabian, A. C. 2012, *MNRAS*, 427, 2998
- Jin, S., Daddi, E., Liu, D., et al. 2018, *ApJ*, 864, 56
- Kennicutt, Robert C., J. 1998, *ApJ*, 498, 541
- Koprowski, M. P., Dunlop, J. S., Michałowski, M. J., et al. 2016, *MNRAS*, 458, 4321
- Lacy, M., Petric, A. O., Sajina, A., et al. 2007, *AJ*, 133, 186
- Lacy, M., Storrie-Lombardi, L. J., Sajina, A., et al. 2004, *ApJS*, 154, 166
- Laigle, C., McCracken, H. J., Ilbert, O., et al. 2016, *ApJS*, 224, 24
- Le Floc'h, E., Aussel, H., Ilbert, O., et al. 2009, *ApJ*, 703, 222
- Lim, C.-F., Chen, C.-C., Smail, I., et al. 2020, *ApJ*, 895, 104
- Liu, D., Lang, P., Magnelli, B., et al. 2019, *ApJS*, 244, 40
- Magdis, G. E., Gobat, R., Valentino, F., et al. 2021, arXiv e-prints, arXiv:2101.04700
- Man, A., & Belli, S. 2018, *Nature Astronomy*, 2, 695
- Man, A. W. S., Greve, T. R., Toft, S., et al. 2016, *The Astrophysical Journal*, 820, 11
- Marchesi, S., Lanzuisi, G., Civano, F., et al. 2016, *ApJ*, 830, 100
- Martig, M., Bournaud, F., Teyssier, R., & Dekel, A. 2009, *ApJ*, 707, 250
- Merlin, E., Fontana, A., Castellano, M., et al. 2018, *MNRAS*, 473, 2098
- Michałowski, M. J., Dunlop, J. S., Koprowski, M. P., et al. 2017, *MNRAS*, 469, 492
- Muzzin, A., Marchesini, D., Stefanon, M., et al. 2013, *ApJ*, 777, 18
- Newman, A. B., Belli, S., Ellis, R. S., & Patel, S. G. 2018, *ApJ*, 862, 125
- Noeske, K. G., Weiner, B. J., Faber, S. M., et al. 2007, *ApJL*, 660, L43
- Ranalli, P., Comastri, A., & Setti, G. 2003, *A&A*, 399, 39
- Sanders, D. B., Salvato, M., Aussel, H., et al. 2007, *ApJS*, 172, 86
- Santini, P., Merlin, E., Fontana, A., et al. 2019, *MNRAS*, 486, 560
- Sargent, M. T., Daddi, E., Bournaud, F., et al. 2015, *ApJL*, 806, L20
- Schreiber, C., Elbaz, D., Pannella, M., et al. 2018a, *A&A*, 609, A30
- Schreiber, C., Labbé, I., Glazebrook, K., et al. 2018b, *A&A*, 611, A22
- Schreiber, C., Glazebrook, K., Nanayakkara, T., et al. 2018c, *A&A*, 618, A85
- Shangguan, J., Ho, L. C., Bauer, F. E., Wang, R., & Treister, E. 2020, *ApJ*, 899, 112
- Simpson, J. M., Smail, I., Wang, W.-H., et al. 2017, *ApJL*, 844, L10
- Simpson, J. M., Smail, I., Swinbank, A. M., et al. 2019, *ApJ*, 880, 43
- Simpson, J. M., Smail, I., Dudzeviciute, U., et al. 2020, arXiv e-prints, arXiv:2003.05484
- Smolčić, V., Zamorani, G., Schinnerer, E., et al. 2009, *ApJ*, 696, 24
- Smolčić, V., Novak, M., Bondi, M., et al. 2017a, *A&A*, 602, A1
- Smolčić, V., Delvecchio, I., Zamorani, G., et al. 2017b, *A&A*, 602, A2
- Somerville, R. S., Hopkins, P. F., Cox, T. J., Robertson, B. E., & Hernquist, L. 2008, *MNRAS*, 391, 481
- Speagle, J. S., Steinhardt, C. L., Capak, P. L., & Silverman, J. D. 2014, *ApJS*, 214, 15
- Straatman, C. M. S., Labbé, I., Spitler, L. R., et al. 2014, *ApJL*, 783, L14

- Szokoly, G. P., Bergeron, J., Hasinger, G., et al. 2004, [ApJS](#), 155, 271
- Toba, Y., Yamashita, T., Nagao, T., et al. 2019, [ApJS](#), 243, 15
- Valentino, F., Tanaka, M., Davidzon, I., et al. 2020, [ApJ](#), 889, 93
- Viero, M. P., Moncelsi, L., Quadri, R. F., et al. 2013, [ApJ](#), 779, 32
- Wagner, A. Y., & Bicknell, G. V. 2011, [ApJ](#), 728, 29
- Wang, W.-H., Lin, W.-C., Lim, C.-F., et al. 2017, [ApJ](#), 850, 37
- Williams, R. J., Quadri, R. F., Franx, M., van Dokkum, P., & Labbé, I. 2009, [ApJ](#), 691, 1879
- Wuyts, S., Labbé, I., Franx, M., et al. 2007, [ApJ](#), 655, 51
- Wuyts, S., Förster Schreiber, N. M., Lutz, D., et al. 2011, [ApJ](#), 738, 106
- Young, L. M., Bureau, M., Davis, T. A., et al. 2011, [MNRAS](#), 414, 940
- Zezas, A. L., Georgantopoulos, I., & Ward, M. J. 1998, [MNRAS](#), 301, 915
- Zhuang, M.-Y., & Ho, L. C. 2020, arXiv e-prints, arXiv:2007.11283